

# Experimental Investigation on the Strength, Deformability, Failure Behavior and Acoustic Emission Locations of Red Sandstone Under Triaxial Compression

Sheng-Qi Yang · Hong-Wen Jing · Shan-Yong Wang

Received: 1 June 2011 / Accepted: 18 November 2011  
© Springer-Verlag 2012

**Abstract** Conventional triaxial compression and “reducing confining pressure” experiments were carried out for red sandstone by an MTS815 Flex Test GT rock mechanics experimental system. Our results show that the post-peak axial deformation characteristics of red sandstone changed as the confining pressure was increased from 5 to 65 MPa. Young’s modulus of red sandstone increased nonlinearly with increasing confining pressure, but Poisson’s ratio remained unaffected. Using our new data, the compactive and dilatant behavior, strength and failure characteristics of sandstone under triaxial compression are further discussed. For our data, the nonlinear Hoek-Brown criterion better reflects the peak strength properties than the linear Mohr-Coulomb criterion. However, the residual strength shows a clear linear relationship with confining pressure, which can be best described using the linear Mohr-Coulomb criterion. The peak and residual strengths were not directly related to the two different loading paths. The onset of dilatancy ( $C'$ ), the switch from compaction-dominated to dilatant-dominated behavior ( $D'$ ) and the stress at zero volumetric strain all increased linearly with the confining pressure. In our conventional triaxial compression experiments, the failure mode changed from mixed tension and shear fracture (single shear fracture) to shear fracture with double slippage planes with

increasing confining pressure. However, the failure mode in our “reducing confining pressure” experiments was more complicated and results mainly from the unstable failure characteristics of the rock during the reduction in confining pressure. Finally, based on our acoustic emission (AE) locations, at a confining pressure of 35 MPa, a detailed analysis of the evolutionary process of internal cracks is presented for the entire loading process.

**Keywords** Red sandstone · Triaxial compression · Strength · Deformation behavior · Failure characteristics · AE locations

## 1 Introduction

Sandstone is a sedimentary rock that is widely used in rock engineering (such as underground engineering, dam base rock engineering and high slope rock engineering, etc.). Furthermore, knowledge of the mechanical behavior of sandstone is important in geotechnical engineering (e.g., the design of waste repositories) and in petroleum geoscience (e.g., the prediction of reservoir deformation and fluid flow). For this reason, in the last few decades, many experimental studies have investigated the mechanical behavior of sandstone, including its strength, deformation behavior, failure characteristics and time-dependent behavior (Wong et al. 1997; Baud et al. 2000; Wu et al. 2000; Klein et al. 2001; Jing et al. 2002; Bésuelle et al. 2003; Fortin et al. 2006; Tembe et al. 2008; Tsai et al. 2008; Zorlu et al. 2008; Heap et al. 2009a, b; Tavallali and Vervoort 2010; Huang et al. 2010; Yang and Jiang 2010; Yang and Jing 2011; Yang et al. 2011).

Uniaxial compression and uniaxial tension tests (or Brazilian tests) are conventional methods that are often

S.-Q. Yang (✉) · H.-W. Jing  
State Key Laboratory for Geomechanics and Deep Underground Engineering, School of Mechanics and Civil Engineering,  
China University of Mining and Technology, 221008 Xuzhou,  
People’s Republic of China  
e-mail: yangsqi@hotmail.com

S.-Y. Wang  
Center for Geotechnical and Materials Modelling,  
The University of Newcastle, University Drive,  
Callaghan, NSW 2238, Australia

used to investigate the strength, deformation behavior and failure characteristics of materials, including rocks. Sandstones, due to the nature of their formation, can be inherently anisotropic (Benson et al. 2005). Al-Harthi (1998) investigated the effect of anisotropy on the uniaxial compressive strength (UCS) of Ranyah sandstone (Saudi Arabia) and found that the strength varied tremendously with orientation (a maximum UCS of 225 MPa and a minimum of 125 MPa). A W-shaped strength anisotropy curve was obtained as a result of plotting the UCS values against the angle between the loading direction and the bedding. Tavallali and Vervoort (2010) conducted indirect uniaxial tension tests on a layered sandstone. They showed that the variation in tensile strength and the failure mode are both a function of the inclination angle between the layer plane and the loading direction. Dynamic cyclic stressing can lead to the degradation of rock physical properties. Heap et al. (2010) performed increasing-amplitude, cyclic-stressing experiments on both Bentheim and Darley Dale sandstone. They found that there is a gradual deterioration in static elastic moduli after each increasing-amplitude cycle. Bagde and Petroš (2005) also performed dynamic uniaxial compressive cyclic-stressing experiments on sandstone. Their experimental results showed that the fatigue strength of their sandstone decreased with loading frequency. Nespereira et al. (2010) carried out petrographic analyses and UCS tests on Salamanca sandstone. They showed that the correlation factor between the mechanical behavior and the petrographic parameters revealed that the cement content is not the only factor governing the UCS, and the composition of the cement may play an important role in the UCS of clay-bearing sandstones. Due to the difficulty of direct tensile testing, Lin et al. (2009) conducted several three-point bending tests on Berea sandstone to study fracture initiation and the associated damage zone by using 2D acoustic emission (AE) locations and electronic speckle pattern interferometry (ESPI). Their experiments indicated that specimen failure was initiated by a large fracture with a localized damage zone.

However, deep underground engineering rock masses, for example, are usually located within triaxial stress state conditions; therefore, it is more relevant to investigate the mechanical characteristics of sandstone under triaxial compression. Wong et al. (1997) studied the transition from brittle faulting and cataclastic flow in six different sandstones. At low confining pressures, shear-induced dilation and brittle faulting were observed. However, at higher confining pressures, shear-enhanced compaction and cataclastic flow were observed. Baud et al. (2000) investigated water-weakening in the cataclastic flow regime on Berea, Boise, Darley Dale and Gosford sandstones. They

found that the presence of water reduced the strength of the sandstones and altered the failure mode at elevated pressures. Heap et al. (2009a) studied time-dependent brittle deformation in Darley Dale sandstone and found that the rate of creep deformation during constant stress experiments was heavily dependent on the applied differential stress. In a later study, Heap et al. (2009b) showed that an increase in temperature from 20 to 75°C increased the rate of creep deformation by up to three orders of magnitude in Darley Dale, Crab Orchard and Bentheim sandstone. Bésuelle et al. (2000) conducted triaxial compression experiments on Vosges sandstone with two slenderness ratios and observed a strong positive dilatancy at lower confining pressures, which decreased and became negative at higher confining pressures. Furthermore, they also analyzed the shear band using X-ray computerized tomography (CT) and scanning electron microscopy (SEM). Feng et al. (2004) studied the damage evolution of sandstone under triaxial compression with chemical corrosion using real-time X-ray CT. They surmised that the CT value is the most important parameter describing the damage evolution process of rock.

AE counts are transient elastic waves generated by the rapid release of energy within a material, such as the strain energy released during microcrack propagation. Monitoring AE during deformation has become an increasingly important diagnostic tool in material science and has provided a wealth of information regarding the failure process in brittle materials (e.g., Lockner et al. 1991; Benson et al. 2007; Fortin et al. 2009; Brantut et al. 2011); it can be used in failure forecasting modeling (e.g., Bell et al. 2011a, b). For instance, Baud et al. (2004) investigated the phenomenon of compaction localization and mechanical deformation of porous sandstone with real-time damage evolution using AE activity. Townend et al. (2008) studied the formation of compaction bands in Diemelstadt sandstone using 3D AE locations recorded by a Hyperion Giga-RAM recorder. Their results demonstrated that compaction bands nucleate at the specimen edge and propagate across the specimen at a rate of 0.08 mm/s. Fortin et al. (2009) investigated shear localization, compaction localization and cataclastic compaction in Bleurswiller sandstone using 3D AE locations. They found that compaction localization and cataclastic compaction generate similar AE signatures to shear localization.

Up to now, most triaxial experiments on sandstone have been performed using the axial displacement rate as the controlling feedback signal. However, since specimen failure in the brittle regime is often very rapid under this mode of control, it is often difficult to obtain reliable post-peak deformation data. In this study, we will attempt to improve our knowledge of post-peak behavior in sandstone using the circumferential displacement rate as

the controlling feedback mechanism. Further, in previous experimental research on sandstone, the effect of the loading path on the strength, failure behavior, crack initiation threshold, crack damage threshold and 3D damage evolution process under triaxial compression are less discussed. To this end, we have performed triaxial experiments on sandstone under two loading paths [i.e., conventional triaxial compression experiments and “reducing confining pressure” experiments (to be described in detail in the next section)] using the circumferential displacement rate as the controlling feedback mechanism. Our research investigates the influence of confining pressure on the deformation parameters of sandstone (in particular, volumetric contraction and dilatancy parameters) to construct a relationship between confining pressure and strength parameters (including peak and residual strength, crack initiation threshold, crack damage threshold and the stress at zero volumetric strain) of sandstone. We also analyze the evolution of damage in our sandstone specimens using the spatial and temporal distribution of AE counts.

## 2 Experimental Material and Testing Procedures

### 2.1 Experimental Material

The material used throughout this study was red sandstone (collected from the Shandong province of China). Red sandstone (Fig. 1) is a fine- to medium-grained, feldspathic sandstone with a connected porosity of 8.8% and a bulk density of 2,360 kg/m<sup>3</sup>. The modal composition is 45% feldspar (with a grain radius of 0.15–0.25 mm), 13.5% quartz (with a grain radius of 0.2–0.3 mm), 31.5% debris (with a grain radius of 0.25–0.4 mm) and 10%

agglutinate (which consisted of gypsum, barite and iron integument).

### 2.2 Testing Equipment

All experiments were performed in an MTS815 Flex Test GT triaxial rock mechanics experimental system (Fig. 2). The maximum loading capacity of the servo-controlled system is 4,700 kN, and the maximum confining pressure is 140 MPa. During experimentation, we measured the axial force (using a load cell with a loading capacity of 2,600 kN) and the axial deformation with an axial Linear Variable Differential Transducer (LVDT) with a range of 5 mm (Fig. 2). The circumferential deformation was measured using an LVDT attached to a chain wrapped tightly around the specimen (Fig. 2), for which the maximum displacement capacity was 8 mm. To eliminate the end friction effects (see Mogi 1966; Hawkes and Mellor 1970), the axial and circumferential LVDT were located in the central part of the specimen (Fig. 2).

### 2.3 Testing Procedure

In this study, we performed a series of triaxial compression experiments using a circumferential displacement rate of 0.06 mm/min. To reiterate, we used the circumferential displacement as the controlling feedback signal (see also Amann et al. 2011; Youn and Tonon 2010) rather than the axial displacement feedback commonly used in rock deformation experiments (see Paterson and Wong 2005). For the purpose of this study, we performed two types of triaxial test: (1) conventional triaxial experiments and (2) “reducing confining pressure” experiments.

The conventional triaxial experiments (Fig. 3a) were carried out under different confining pressures of 5, 20, 35,

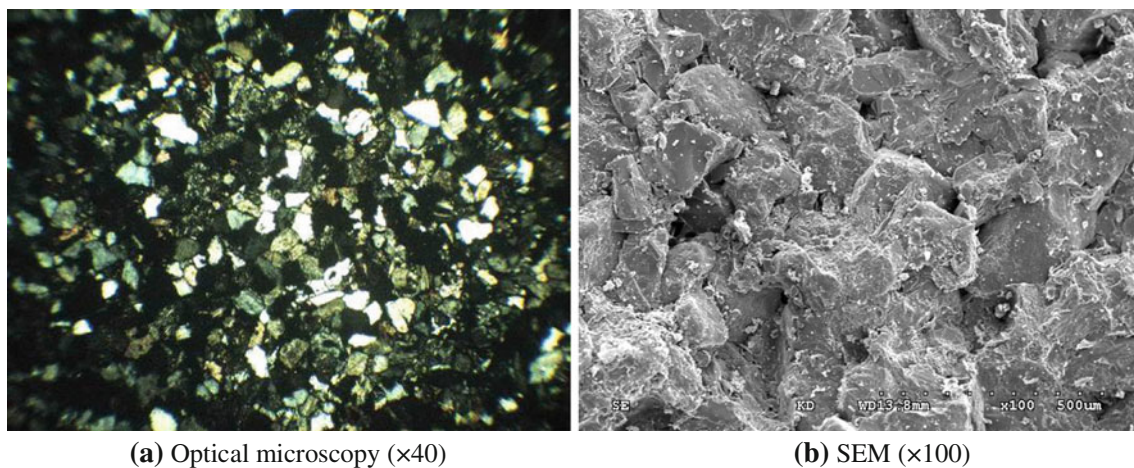


**Fig. 1** Optical microscopy and SEM photomicrographs of red sandstone

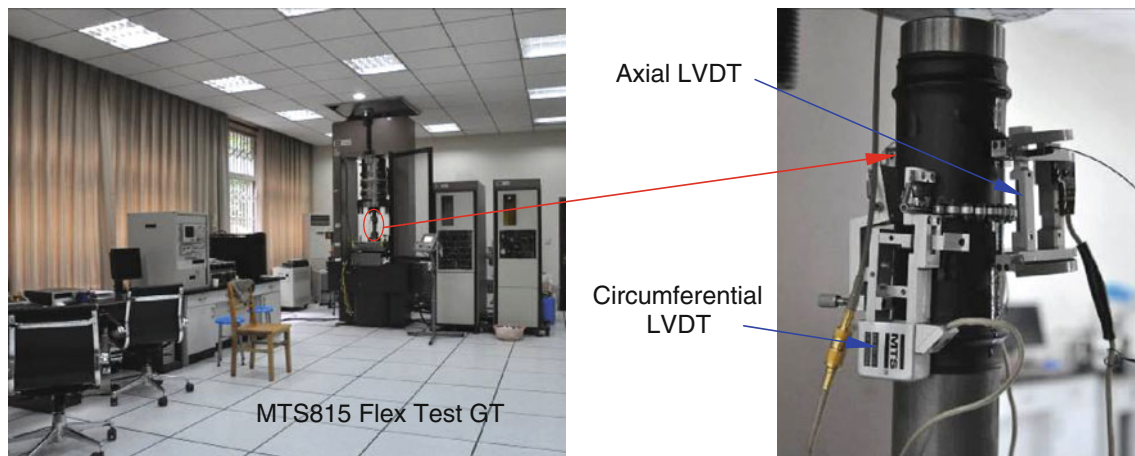


**Fig. 2** MTS815 Flex Test GT triaxial rock mechanics experimental system and strain measurement

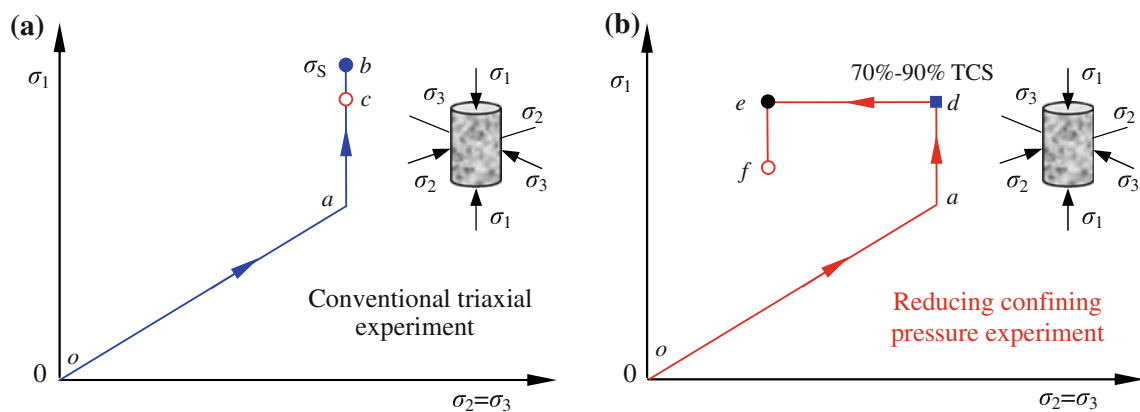


**Fig. 3** The two different loading paths used in this study, presented in the principal stress space ( $\sigma_3$ ,  $\sigma_1$ ). Conventional triaxial experiment:  $oa \rightarrow ab \rightarrow bc$ ; “reducing confining pressure experiment”:  $oa \rightarrow ad \rightarrow de \rightarrow ef$

50 and 65 MPa, and consisted of the following two steps. Firstly, the confining pressure was increased to the desired value at a constant rate of 0.1 MPa/s [to ensure that the specimen was under uniform hydrostatic stresses ( $oa$ )]. Finally, the deviatoric stress ( $ab \rightarrow bc$ ) was applied to the surface of the specimen at a constant circumferential displacement rate of 0.06 mm/min until failure.

Our “reducing confining pressure” experiments (Fig. 3b) were conducted using the following three steps. First, the hydrostatic pressure was applied to the specimen at a rate of 0.1 MPa/s until the desired value was reached ( $oa$ ). The deviatoric stress was applied up to a pre-determined level [either 70 or 90% of the triaxial compressive strength (TCS) determined from our conventional triaxial tests] at a constant circumferential displacement control rate of 0.06 mm/min ( $ad$ ). Finally, the major principal stress ( $\sigma_1$ ) was kept constant, but the confining pressure

was reduced at a rate of 0.1 MPa/s until the specimen failure occurred ( $de \rightarrow ef$ ).

All triaxial experiments were carried out on cylindrical specimens 50 mm in diameter and 100 mm in length in accordance with the ISRM standard (Fairhurst and Hudson 1999). The specimens were all cored from the same large rectangular block and in the same orientation. All the experiments were performed on dry specimens at room temperature.

#### 2.4 AE Measuring Procedure

As is well known, the AE technique is predominantly related to the release of elastic energy within rock materials. AE hits and/or energy often monitored to detect the onset (termed  $C'$ , see Wong et al. 1997) and the evolution of microcracking, and to analyze the spatial and temporal



progression of internal cracks (e.g., Lockner et al. 1991). In this study, the output of AE was recorded by a PCI-2 AE 3D measuring system made by Physical Acoustic Corp. (PAC) using eight AE sensors with a frequency of 6 kHz. The amplitude threshold of the sensors was set to 33 dB.

### 3 Triaxial Experimental Results of Red Sandstone

#### 3.1 Deformation Behavior Under Conventional Triaxial Compression

The triaxial stress-strain curves for red sandstone under a variety of confining pressures are presented in Figs. 4 and 5. The synopsis plots of Fig. 5 demonstrate that an increase in confining pressure served to increase the strength (in a similar manner as observed previously, see Heap et al. 2009a). In all cases, even at the highest confining pressure of 65 MPa, the failure mode remained brittle (i.e., the ability of the rock to resist load decreases with permanent strain, see Rutter 1986). However, there is an observable change in the post-peak behavior with increasing confining pressure. Post-peak behavior switched from class I (the slope of the post-peak stress-strain curve is negative, see Wawersik and Fairhurst 1970) at a confining pressure of 5 MPa to class II (where the slope is positive) at confining pressures above 5 MPa. Further, there was a gradual increase in strain-softening behavior, and the magnitude of the stress drop was reduced with increasing confining pressure. The influence of confining pressure on the deformation parameters is described in more detail in Sect. 3.3.

The stress-strain curve at 5 MPa (Fig. 4a) shows initially a non-linear (concave) deformation, usually attributed to the closure of pre-existing microcracks. Our data suggest that this stage of microcrack closure was dependent on the confining pressure. At lower confining pressures (e.g., Fig. 4a, b), the stage of microcrack closure was more distinct than at higher confining pressures (e.g., Fig. 4d, e). This is likely to be a result of the confining pressure acting to close the pre-existing microcracks prior to the start of deformation. Following the period of microcrack closure (if present) the specimens deformed elastically (the pseudo-linear portions of the stress-strain curves). The departure from pseudo-linear behavior marked the yield point of the specimens and where they entered a phase of strain hardening. Once the peak stress was reached there was a stage of strain softening (that increased with increasing confining pressure); finally, the specimens failed.

The evolution of the volumetric strain during a typical experiment is shown in Fig. 4f. The volumetric strain was

characterized by an initial phase of compaction-dominated behavior followed by a phase of dilatancy-dominated behavior. The onset of dilatancy can be identified as the stress where the volumetric strain departed from pseudo-linear elastic behavior (this is commonly referred to as  $C'$ , see Wong et al. 1997). After point A, compaction was in direct competition with dilatancy (although the specimen was still in net compaction). Eventually, the rate of compaction and dilatancy became equal, resulting in an inflection point in the volumetric strain curve (this is commonly referred to as  $D'$ , see Heap et al. 2009a). This is marked as point B on Fig. 4f and marks the point where the deformation of the specimen switched from compaction-dominated to dilatancy-dominated. As the stress was increased further, more and more microcracking occurred, and the specimen continued to dilate. The volumetric strain eventually passed back through zero strain ( $\sigma_{v0}$ ) before it continued to increase until specimen failure. Table 1 lists the axial and circumferential strain of red sandstone at  $C'$ ,  $D'$  and the stress at zero volumetric strain under conventional triaxial compression.

To investigate the reproducibility of our experimental setup and our experimental material, we performed a new experiment at a confining pressure of 35 MPa. Figure 4c shows the axial stress-strain curves for two red sandstone specimens, RS-a03<sup>#</sup> and RS-a07<sup>#</sup> (after the peak stress, specimen RS-a07<sup>#</sup> was unloaded at point F). The stress-strain curves and the peak stress were nearly identical, adding to the veracity of our data set.

Figure 6 shows the influence of confining pressure (Fig. 6a) and specimen variability (Fig. 6b) on the relationship between the circumferential strain and the axial strain of red sandstone prior to the peak stress. Firstly, it can be seen that the circumferential strain increased non-linearly with the axial strain. At lower stress levels, the circumferential strain increased slowly with the axial strain, but at higher stress levels, the rate of circumferential strain was higher than that of axial strain. The confining pressure and specimen variability had no obvious influence on the relationship between the circumferential strain and the axial strain at the lower stress levels. However, at higher stress levels, the rate of circumferential strain with axial strain was smaller at higher confining pressures (Fig. 6a). This suggests that higher confining pressures suppressed the circumferential deformation of the specimens. We observed only a small deviation in the circumferential-axial strain curves for two specimens deformed under the same pressure conditions (Fig. 6b), again adding to the veracity of our data set.

Figure 6 also indicates that Poisson's ratio was not a constant and that it changed with the axial deviatoric stress. Thus, it was more difficult to determine Poisson's ratio because of obvious nonlinearity between the

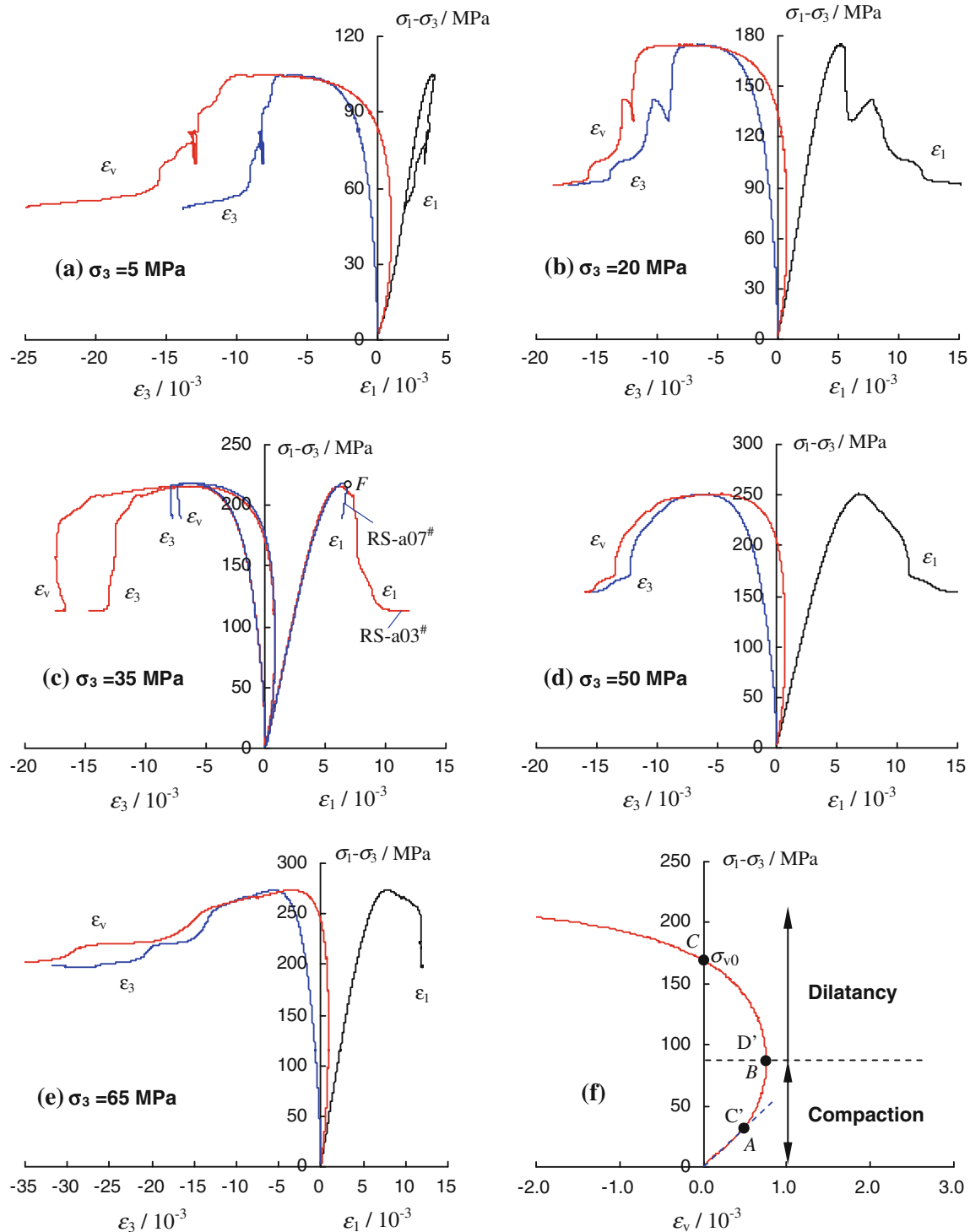


**Fig. 4** Stress-strain curves for red sandstone from conventional triaxial compression experiments.  $\epsilon_1$  and  $\epsilon_3$  represent the axial and circumferential strain, respectively.  $\epsilon_v$  refers to the volumetric strain,

which is calculated from the sum of the axial strain and twice the circumferential strain (i.e.,  $\epsilon_v = \epsilon_1 + 2\epsilon_3$ )

circumferential strain and the axial strain, even though it was observed during elastic deformation. Therefore, in this study, we calculated Poisson's ratio using the following

method. We used the average of the absolute value of the ratio of circumferential strain and axial strain in the range of axial differential stress from 30% to 70% TCS, as shown

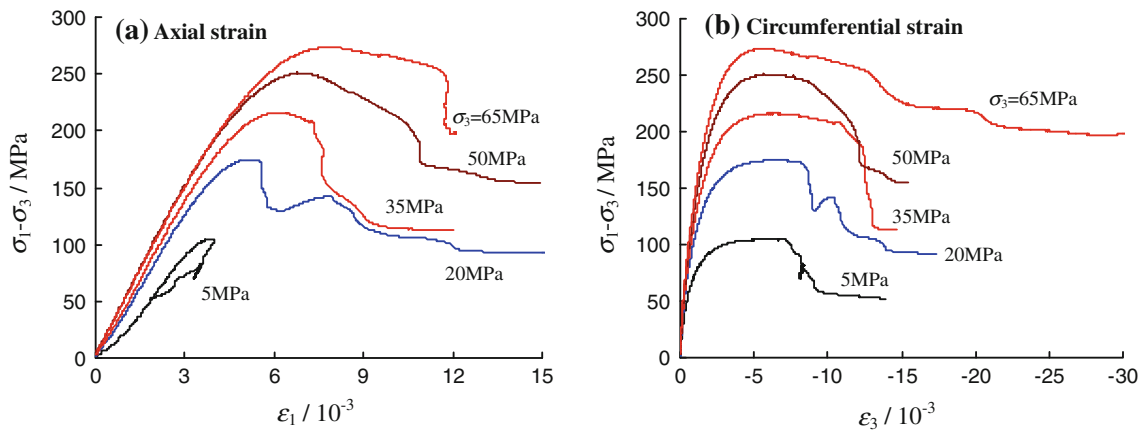


**Fig. 5** The influence of confining pressure on the relationship between axial deviatoric stress and axial strain, and between axial deviatoric stress and circumferential strain for red sandstone

**Table 1** Axial and circumferential strain of red sandstone at  $C'$ ,  $D'$  and the stress at zero volumetric strain from conventional triaxial compression experiments

$\sigma_3/\text{MPa}$	$\varepsilon_{1c}/10^{-3}$	$\varepsilon_{3c}/10^{-3}$	$\varepsilon_{1d}/10^{-3}$	$\varepsilon_{3d}/10^{-3}$	$\varepsilon_{1v0}/10^{-3}$	$\varepsilon_{3v0}/10^{-3}$
5	0.51	-0.03	1.65	-0.34	2.79	-1.39
20	0.53	-0.06	1.62	-0.43	3.20	-1.60
35 (RS-a03 <sup>#</sup> )	0.60	-0.09	1.73	-0.49	3.80	-1.90
35 (RS-a07 <sup>#</sup> )	0.58	-0.06	1.98	-0.60	4.04	-2.02
50	0.62	-0.12	2.08	-0.71	4.30	-2.15
65	0.68	-0.12	2.74	-0.94	5.49	-2.74

$\varepsilon_{1c'}$  and  $\varepsilon_{3c'}$  represent the axial and circumferential strain at  $\sigma_{c'}$ , respectively.  $\varepsilon_{1d'}$  and  $\varepsilon_{3d'}$  represent the axial and circumferential strain at  $\sigma_{d'}$ , respectively.  $\varepsilon_{1v0}$  and  $\varepsilon_{3v0}$  represent the axial and circumferential strain at  $\sigma_{v0}$ , respectively

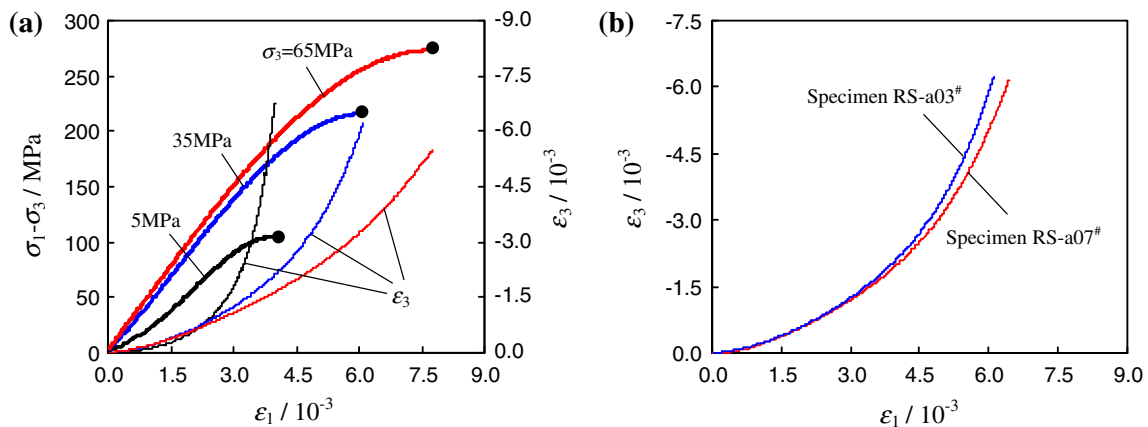


**Fig. 6** Relationship between the circumferential strain and the axial strain of red sandstone prior to the peak stress: **a** the effect of confining pressure and **b** the effect of specimen variability. The filled black circles represent the peak stress of the specimen

in Table 2, which lists Young's modulus, Poisson's ratio and the peak strain of red sandstone from our conventional triaxial compression experiments.  $E_s$  and  $E_{50}$  represent the elastic modulus and the deformation modulus of the

sandstone (Yang and Jiang 2010), respectively.  $\nu$  represents Poisson's ratio of rock.  $\varepsilon_{1c}$ ,  $\varepsilon_{3c}$  and  $\varepsilon_{vc}$  are respectively defined as the axial, circumferential and volumetric strain values at the peak stress.

**Table 2** Young's modulus, Poisson's ratio and peak strain of red sandstone from conventional triaxial compression experiments

$\sigma_3/\text{MPa}$	$E_s/\text{GPa}$	$E_{50}/\text{GPa}$	$\nu$	$\varepsilon_{1c}/10^{-3}$	$\varepsilon_{3c}/10^{-3}$	$\varepsilon_{vc}/10^{-3}$
5	35.9	27.4	0.28	3.99	-6.77	-9.54
20	44.6	42.0	0.34	5.18	-6.49	-7.77
35 (RS-a03 <sup>#</sup> )	47.3	46.3	0.36	6.10	-6.22	-6.33
35 (RS-a07 <sup>#</sup> )	46.9	45.4	0.34	6.43	-6.16	-5.89
50	51.0	51.6	0.37	6.77	-5.67	-4.57
65	50.1	50.7	0.34	7.75	-5.48	-3.20

### 3.2 Deformation Behavior in “Reducing Confining Pressure” Experiments

Reducing the confining pressure during a triaxial compression experiment can also lead to specimen failure (Yang et al. 2011), which is different from the path of a conventional triaxial compression experiment (as in Fig. 3). Figure 7 shows the results from triaxial experiments where

the confining pressure was reduced upon reaching a pre-determined high percentage of the short-term failure stress of red sandstone (as determined by conventional triaxial experiments). For comparison, the stress-strain curves from these experiments are plotted together with those from conventional triaxial experiments under the same confining pressure. It can be seen that, between the point where the confining pressure reduction was initiated and the failure of

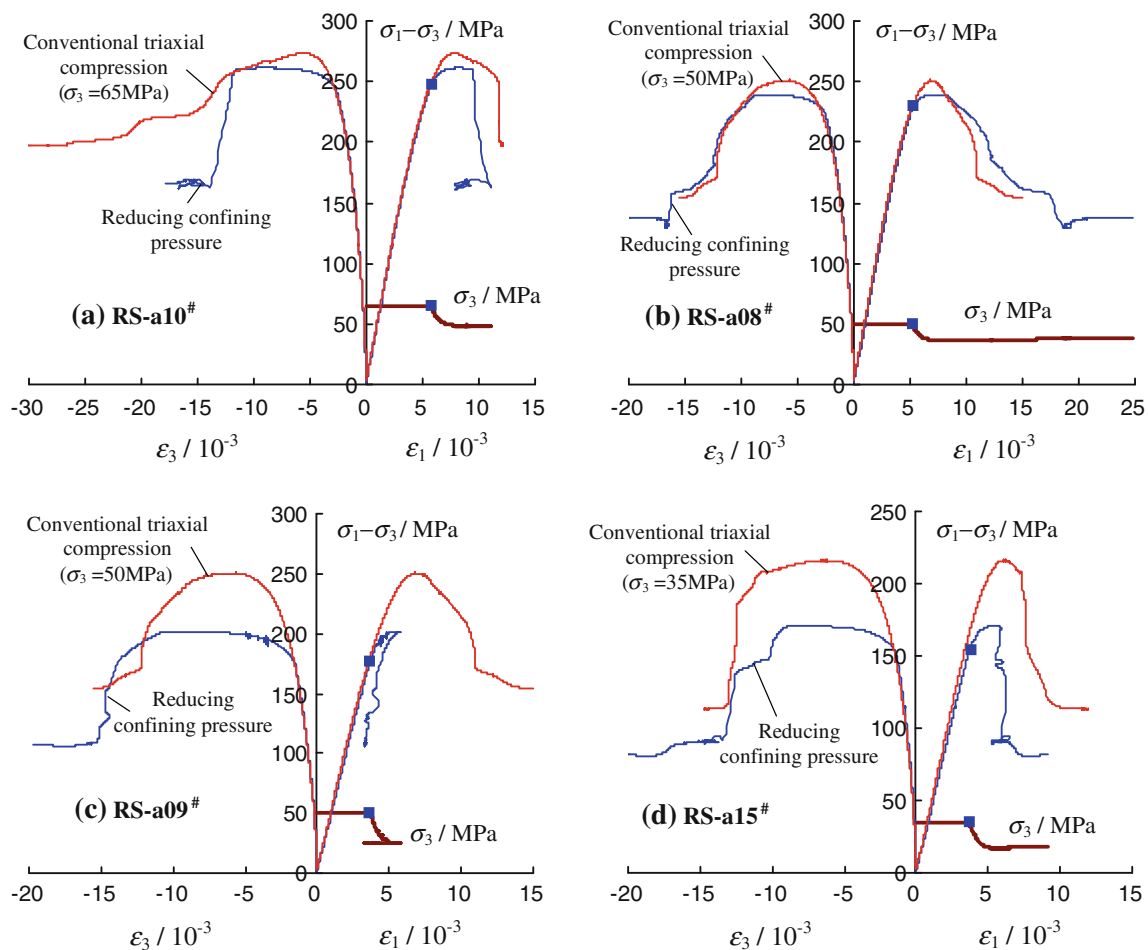


**Fig. 7** Results from conventional triaxial experiments and “reducing confining pressure” experiments. The *filled squares* represent the position where the confining pressure was reduced



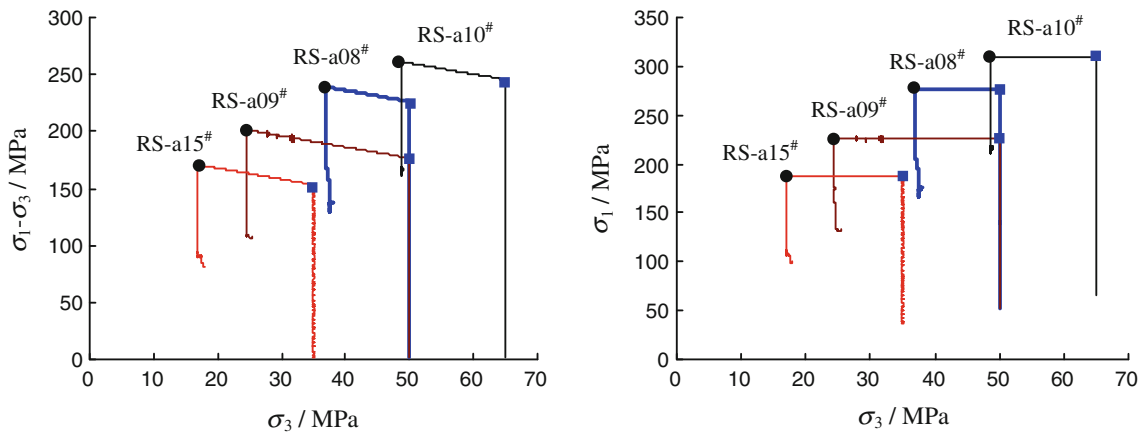


**Fig. 8** Relationship among axial differential stress, axial stress and confining pressure for red sandstone in our “reducing confining pressure” experiments (see text for details). The *filled squares*

represent the position where the confining pressure was reduced, and the *filled circles* indicate the failure point of the specimen

the specimen, the axial deviatoric stress still increased, even when  $\sigma_1$  was kept constant (Fig. 8). After failure, the axial supporting capacity dropped rapidly to the value of the residual strength.

In Fig. 7a, the initial confining pressure  $\sigma_{3i}$  of specimen RS-a10<sup>#</sup> was 65 MPa. The axial deviatoric stress was then increased and kept at approximately 90% of the TCS at  $\sigma_3 = 65$  MPa. At this stress level, the confining pressure was reduced and specimen failure occurred at a confining pressure of 48.7 MPa ( $\sigma_{3f}$ ). Specimen RS-a08<sup>#</sup> (Fig. 7b) had an initial confining pressure of 50 MPa and was also loaded to 90% of the TCS (although this time 90% of the peak stress at  $\sigma_3 = 50$  MPa). Specimen RS-a08<sup>#</sup> failed at a confining pressure of 36.8 MPa, which was lower than for the previous experiment with an initial confining pressure of 65 MPa. The analysis shows that for lower  $\sigma_{3i}$ , the  $\sigma_{3f}$  was lower for specimens held at the same percentage of the TCS.

Specimen RS-a09<sup>#</sup> ( $\sigma_{3i} = 50$  MPa and held at 70% of the TCS at  $\sigma_3 = 50$  MPa) failed at a confining pressure of 24.5 MPa (Fig. 7c), which was lower than the value for RS-a08<sup>#</sup> ( $\sigma_{3i} = 50$  MPa and held at 90% of the TCS at  $\sigma_3 = 50$  MPa). So, if the initial confining pressure was the same, increasing the percentage of the failure stress acted

to reduce the confining pressure at which the specimen failed. Specimen RS-a15<sup>#</sup> ( $\sigma_{3i} = 35$  MPa and held at 70% of the TCS at  $\sigma_3 = 35$  MPa) failed at a confining pressure of 17 MPa (Fig. 7d). The deformation parameters, as in Tables 1 and 2, are listed for these experiments in Tables 3 and 4.

### 3.3 Influence of the Confining Pressure on the Deformation Parameters

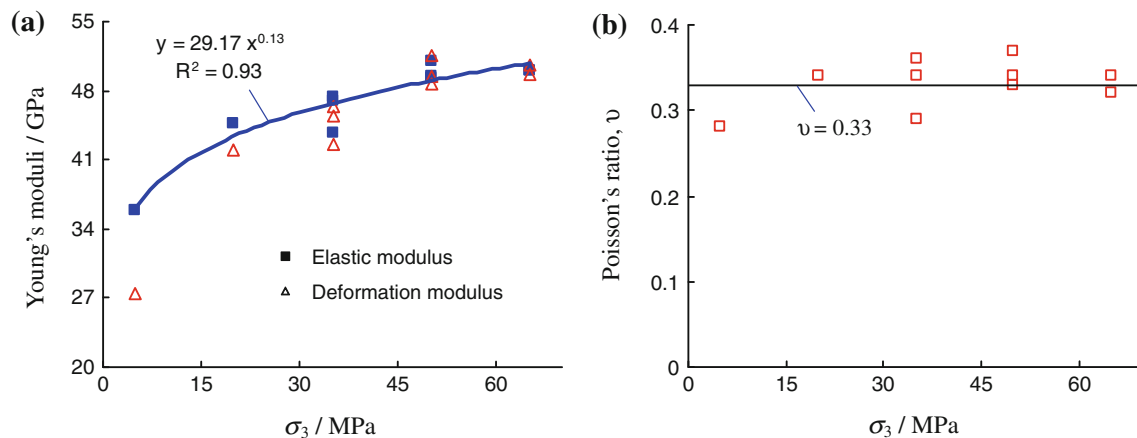
Using the deformation parameters listed in Tables 1, 2, 3 and 4, the relationship between the deformation parameters of red sandstone and the confining pressure can now be investigated. Figure 9 illustrates the influence of the confining pressure on Young’s modulus and Poisson’s ratio. It can be seen that Young’s modulus of red sandstone increased nonlinearly with increasing confining pressure. At  $\sigma_3 = 5$  MPa, the elastic modulus and the deformation modulus were 35.9 and 27.4 GPa, respectively. Whereas when  $\sigma_3$  was increased to 50 MPa, the elastic modulus and the deformation modulus were increased to 51.0 and 51.6 GPa, respectively. At pressures above 50 MPa, Young’s modulus remained constant. Furthermore, the difference between the elastic modulus and the deformation

**Table 3** Young’s modulus, Poisson’s ratio and peak strain of red sandstone in our “reducing confining pressure” experiments (see text for details)

Specimen	$\sigma_{3i}$ /MPa	$\sigma_{3f}$ /MPa	$E_s$ /GPa	$E_{50}$ /GPa	$\nu$	$\varepsilon_{1c}/10^{-3}$	$\varepsilon_{3c}/10^{-3}$	$\varepsilon_{vc}/10^{-3}$
RS-a10 <sup>#</sup>	65	48.7	50.1	49.7	0.32	8.15	−8.79	−9.42
RS-a08 <sup>#</sup>	50	36.8	49.3	48.7	0.33	7.18	−7.75	−8.32
RS-a09 <sup>#</sup>	50	24.5	49.5	49.4	0.34	5.61	−9.04	−12.5
RS-a15 <sup>#</sup>	35	17.0	43.8	42.6	0.29	5.49	−7.69	−9.89

**Table 4** Axial and circumferential strain of red sandstone at  $C'$ ,  $D'$  and the stress at zero volumetric strain in our “reducing confining pressure” experiments (see text for details)

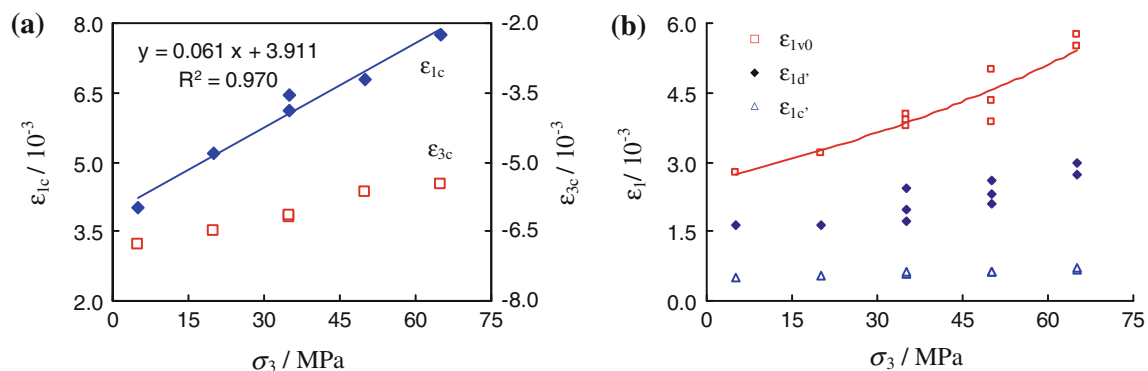
Specimen	$\sigma_{3i}/\text{MPa}$	$\sigma_{3f}/\text{MPa}$	$\varepsilon_{1c'}/10^{-3}$	$\varepsilon_{3c'}/10^{-3}$	$\varepsilon_{1d'}/10^{-3}$	$\varepsilon_{3d'}/10^{-3}$	$\varepsilon_{1v0}/10^{-3}$	$\varepsilon_{3v0}/10^{-3}$
RS-a10 <sup>#</sup>	65	48.7	0.72	−0.14	2.99	−1.00	5.73	−2.87
RS-a08 <sup>#</sup>	50	36.8	0.63	−0.10	2.59	−0.84	5.01	−2.51
RS-a09 <sup>#</sup>	50	24.5	0.63	−0.11	2.31	−0.74	3.85	−1.93
RS-a15 <sup>#</sup>	35	17.0	0.63	−0.08	2.42	−0.68	3.91	−1.96

**Fig. 9** Influence of the confining pressure on Young's modulus and Poisson's ratio of red sandstone

modulus tended to decrease as  $\sigma_3$  was increased, which was the result of the more pronounced stage of microcrack closure at lower confining pressures. At  $\sigma_3 = 35$  MPa, Young's modulus showed a slight variation, the result of natural specimen variability between specimens cored from the same block. However, at higher confining pressures of 50 and 65 MPa, the effect of specimen variability on Young's modulus was significantly reduced. Poisson's ratio of red sandstone was unaffected by confining pressure (Fig. 9b). In the range of tested  $\sigma_3$ , Poisson's ratio varied from 0.28 to 0.37, and the average of Poisson's ratio was

approximately 0.33. Thus, the dispersion extent (the ratio of the  $D$  value between the maximum value and the minimum value to the average value) was approximately 27.3%.

The influence of  $\sigma_3$  on the corresponding strains (listed in Tables 1, 2, 3 and 4) is presented in Fig. 10. We can conclude that the peak axial strain of red sandstone increased linearly, but the peak circumferential strain had a slight decreasing trend as a function of increasing  $\sigma_3$  (Fig. 10a). Furthermore, the sensitivity of the peak axial strain on  $\sigma_3$  was higher than that of the peak circumferential strain. However, in “reducing confining pressure” experiments,

**Fig. 10** Influence of the confining pressure on the corresponding strains (listed in Tables 1, 2, 3, 4) in red sandstone

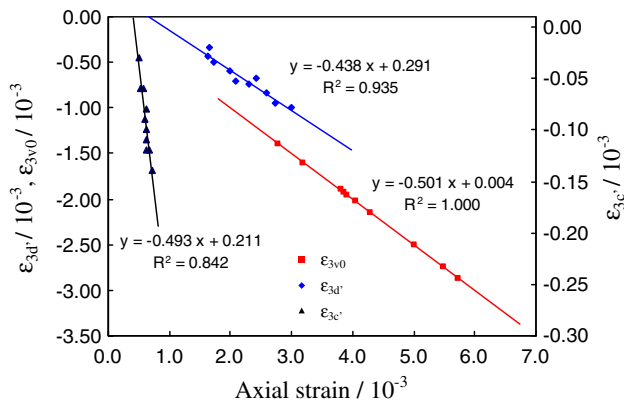


**Fig. 11** Relationship between the axial strain and the circumferential strain of red sandstone at  $C'$ ,  $D'$  and the stress of zero volumetric strain

the peak strains had no clear linear relationship, especially for the peak circumferential strain. Also, the peak strain in our “reducing confining pressure” experiments was higher than that for our conventional triaxial compression experiments, for the same confining pressure.

Based on the data listed in Tables 1 and 4, the effect of  $\sigma_3$  on the axial and circumferential strains at  $C'$ ,  $D'$  and the stress at zero volumetric strain will now be discussed (Fig. 10b). From Fig. 10b, it can be seen that  $\varepsilon_{1c'}$ ,  $\varepsilon_{1d'}$  and  $\varepsilon_{1v0}$  all increased nonlinearly with increasing  $\sigma_3$ , which was different from the effect of  $\sigma_3$  on the peak axial strain. In detail, the sensitivity of  $\sigma_3$  on  $\varepsilon_{1v0}$  was higher than that for  $\varepsilon_{1d'}$ , while the sensitivity of  $\sigma_3$  on  $\varepsilon_{1d'}$  was higher than that for  $\varepsilon_{1c'}$ .

Figure 11 illustrates the relationship between the axial strain and the circumferential strain at  $C'$ ,  $D'$  and the stress of zero volumetric strain. From Fig. 11, we can conclude that the  $\varepsilon_{3c'}$ ,  $\varepsilon_{3d'}$  and  $\varepsilon_{3v0}$  of red sandstone increased linearly with increasing  $\varepsilon_{1c'}$ ,  $\varepsilon_{1d'}$  and  $\varepsilon_{1v0}$ , respectively.

#### 4 Strength and Failure Behavior of Red Sandstone

The linear Mohr-Coulomb criterion can be expressed in terms of the maximum axial supporting capability  $\sigma_S$  and

the minimum principal stress  $\sigma_3$  (i.e., confining pressure) (Mohr 1914; Yang et al. 2011):

$$\sigma_S = \sigma_0 + q\sigma_3 \quad (1)$$

where  $\sigma_0$  is usually regarded as the UCS of rock material. The  $\sigma_0$  and  $q$  are related to the cohesion  $c$  and the internal friction angle  $\varphi$  of rock material, which can be expressed in the following forms, respectively:

$$\sigma_0 = 2c \cos \varphi / (1 - \sin \varphi) \quad (2)$$

$$q = (1 + \sin \varphi) / (1 - \sin \varphi) \quad (3)$$

The Hoek-Brown criterion is an empirical strength criterion that has been widely applied in rock mechanics and engineering. The basic equation describing the peak triaxial compressive strength of a wide range of isotropic rock materials can be written as (Hoek and Brown 1980, 1997):

$$\sigma_S = \sigma_3 + (m\sigma_c\sigma_3 + s\sigma_c^2)^{0.5} \quad (4)$$

where  $\sigma_c$  is the UCS of the intact rock material, and  $m$  and  $s$  are all material constants for a specific rock. When the parameter  $m$  is larger, the rock is stronger. The parameter  $s$  reflects the fractured extent, ranging from 0 to 1. When the parameter  $s$  is closer to 1, the rock is more intact.

##### 4.1 Peak Strength and Residual Strength Behavior

Tables 5 and 6 list the peak stress ( $\sigma_p$ ) and the residual strength ( $\sigma_{cr}$ ) values for red sandstone from our conventional triaxial compression experiments (obtained from the stress-strain curves of Figs. 4, 5). Over the entire confining pressure range,  $\sigma_S$  increased from 110.1 to 338.6 MPa and  $\sigma_{sr}$  from 57 to 262.6 MPa. These findings are different from those for Vosges sandstone (Bésuelle et al. 2000), i.e., the peak strength decreased with increasing confining pressure within the range 50–60 MPa.

By adopting the linear Mohr-Coulomb criterion (Eq. 1) and the nonlinear Hoek-Brown criterion (Eq. 4), the influence of  $\sigma_3$  on the peak strength of red sandstone under triaxial compression can be presented as in Fig. 12. From Fig. 12, we can see that the peak strength of red sandstone

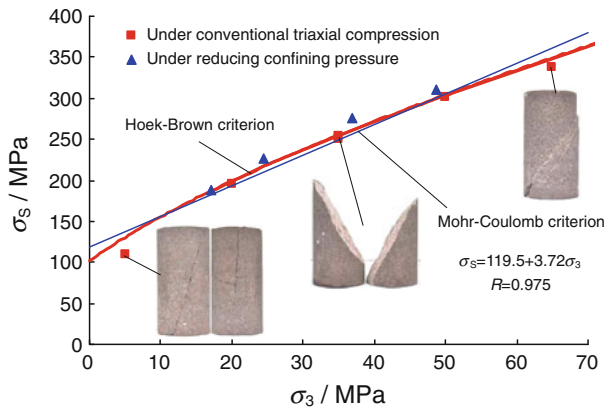
**Table 5** Peak strength and residual strength values for red sandstone in conventional triaxial compression experiments

$\sigma_3$ /MPa	$\sigma_{cr}$ /MPa	$\sigma_p$ /MPa	$\sigma_{sr}$ /MPa	$\sigma_S$ /MPa	Failure mode
5	52.0	105.1	57.0	110.1	Mixed tension and shear fracture
20	91.3	174.7	111.3	194.7	Mixed tension and shear fracture
35 (RS-a03 <sup>#</sup> )	113.2	216.1	148.2	251.1	Single shear fracture
35 (RS-a07 <sup>#</sup> )	—	218.0	—	253.0	—
50	154.3	251.2	204.3	301.2	Shear fracture with local slippage lines
65	197.6	273.6	262.6	338.6	Shear fracture with double slippage planes

$$\sigma_S = \sigma_p + \sigma_3; \sigma_{sr} = \sigma_{cr} + \sigma_3$$

**Table 6** Peak strength and residual strength values for red sandstone in our “reducing confining pressure” experiments (see text for details)

Specimen	$\sigma_{3i}$ /MPa	$\sigma_{3f}$ /MPa	$\sigma_{cr}$ /MPa	$\sigma_p$ /MPa	$\sigma_{sr}$ /MPa	$\sigma_s$ /MPa	Failure mode
RS-a10 <sup>#</sup>	65	48.7	164	261.2	212.7	309.9	Shear fracture with local tension crack
RS-a08 <sup>#</sup>	50	36.8	133	239.2	169.8	276.0	Complicated fracture
RS-a09 <sup>#</sup>	50	24.5	106	201.4	130.5	225.9	Complicated fracture
RS-a15 <sup>#</sup>	35	17.0	81	170.7	98.0	187.7	Complicated fracture

**Fig. 12** Peak strength analysis of red sandstone under triaxial compression. The symbols represent the experimental results, and the lines represent the theoretical values in accordance with the Mohr-Coulomb or Hoek-Brown criterion. ( $R$  is the correlation coefficient of determination of the regression)

under triaxial compression possessed a distinctly non-linear behavior with increasing  $\sigma_3$ , which indicates that the non-linear Hoek-Brown criterion reflects the peak strength properties better than the linear Mohr-Coulomb criterion. With an increase of confining pressure, the failure mode of red sandstone (Fig. 12) changed from mixed tension and shear fracture (single shear fracture) to shear fracture with double slippage planes, which further testified to the fact that the non-linear Hoek-Brown criterion is more suitable for use on our data. Moreover, the linear Mohr-Coulomb criterion predicts the peak strength to be higher than its measured value at low and high confining pressures, and lower at intermediate confining pressures (Fig. 12).

It can also be seen that the peak strength of red sandstone was not directly dependent on the loading path (Fig. 12), meaning that our “reducing confining pressure” experiments can also be used to obtain the strength behavior of the rock. Note that, at a confining pressure of 35 MPa, the difference in the peak strength was only 1.9 MPa for two different curves. Table 7 presents more details on the peak strength parameters of red sandstone using the non-linear Hoek-Brown criterion. In Table 7, the parameters  $\sigma_c$  and  $m$  are back-calculated by assuming  $s = 1.000$ . The parameters  $\sigma_c$  and  $m$  are a little higher for the “reducing confining pressure” experiments than for the

conventional triaxial compression experiments. However, the uniaxial compressive strength  $\sigma_c$  (back-calculated using the non-linear Hoek-Brown criterion) was distinctly higher than the measured value of about 70 MPa obtained from a uniaxial compressive experiment.

The residual strength parameters of red sandstone under triaxial compression using the linear Mohr-Coulomb criterion are presented in Table 8 and Fig. 13. Good linear regression coefficients of  $R = 0.995$  and  $0.999$  were determined for the conventional triaxial experiments and the “reducing confining pressure” experiments, respectively. Even though there was an obvious non-linear relationship between the peak strength and the confining pressure, the residual strength clearly had a linear relation with  $\sigma_3$  (Fig. 13). Moreover, this relationship was not dependent on the loading path, which results mainly from supporting the axial capacity of the sandstone by friction slippage at the residual strength stage. Thus, the residual cohesion values for red sandstone, obtained for two different loading paths, were all approximately 10.6 MPa. Also, the difference in the residual internal friction angle between our conventional triaxial compression tests and our “reducing confining pressure” tests was very small (only  $1.3^\circ$ ) and can therefore be ignored in in situ engineering practices.

Table 9 shows the peak strength parameters of red sandstone obtained using the linear Mohr-Coulomb criterion. Comparing these values with those of Table 8, it is clear that the peak cohesion of red sandstone was 28.36 MPa for our conventional triaxial compression tests and 32.63 MPa for our “reducing confining pressure” tests (which are both considerably higher than residual cohesion of  $\sim 10.6$  MPa). However, the peak internal friction angle (which has an average value of  $35.7^\circ$ ) obtained from the two different loading paths was very close to the residual internal friction angle (which has an average value of  $33.5^\circ$ ).

#### 4.2 $C'$ , $D'$ and the Stress at Zero Volumetric Strain

$C'$ ,  $D'$  and the stress at zero volumetric strain for red sandstone under triaxial compression are listed in Table 10. It can be seen that, over the whole range of tested pressures (5–65 MPa),  $\sigma_{c'}$  varied from 10.2 to 37.3 MPa,  $\sigma_{d'}$  from

**Table 7** Peak strength parameters of red sandstone using the non-linear Hoek-Brown criterion

Loading path	UCS/MPa	$\sigma_c$ /MPa	$m$	$s$	$a$	$R$
Conventional triaxial compression	70	90.8	11.76	1.000	0.5	0.995
“Reducing confining pressure”	70	97.4	12.71	1.000	0.5	0.994
United regression for all of the specimens	70	101.7	10.66	1.000	0.5	0.980

**Table 8** Residual strength parameters of red sandstone in using the linear Mohr-Coulomb criterion

Loading path	$\sigma_0$ /MPa	$q$	$c$ /MPa	$\varphi$ /(°)	$R$
Conventional triaxial compression	39.03	3.36	10.65	32.8	0.995
“Reducing confining pressure”	39.94	3.55	10.60	34.1	0.999

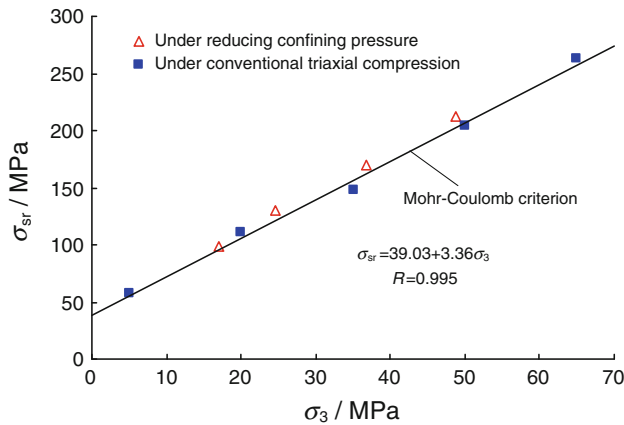


**Fig. 13** Residual strength analysis of red sandstone under triaxial compression. All of the *symbols* represent the experimental results, and the *lines* represent the theoretical values in accordance with Mohr-Coulomb criterion. ( $R$  is the correlation coefficient of determination of the linear regression)

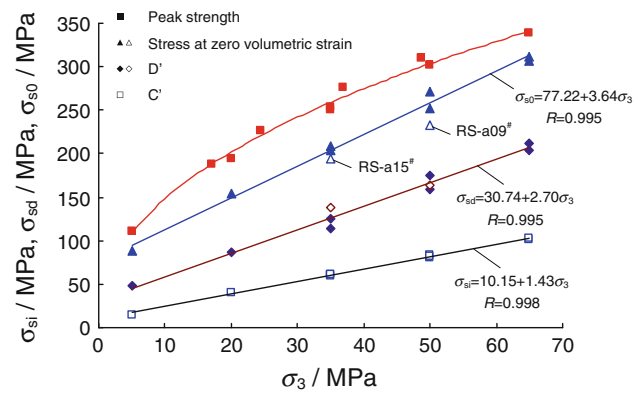


**Fig. 14** The influence of the confining pressure on  $C'$ ,  $D'$  and the stress at zero volumetric strain under triaxial compression. The *symbols* represent the experimental results, and the *curves* represent the theoretical values found using the Mohr-Coulomb criterion

**Table 9** Peak strength parameters of red sandstone using the linear Mohr-Coulomb criterion

Loading path	$\sigma_0$ /MPa	$q$	$c$ /MPa	$\varphi$ /(°)	$R$
Conventional triaxial compression	110.0	3.76	28.36	35.4	0.985
“Reducing confining pressure”	127.9	3.84	32.63	35.9	0.995
United regression for all the specimens	119.5	3.72	30.98	35.2	0.975

**Table 10**  $C'$ ,  $D'$  and the stress at zero volumetric strain for red sandstone under triaxial compression

$\sigma_3$ /MPa	$\sigma_c$ /MPa	$\sigma_d$ /MPa	$\sigma_{v0}$ /MPa	$\sigma_{si}$ /MPa	$\sigma_{sd}$ /MPa	$\sigma_{s0}$ /MPa
5	10.2	43.2	83.5	15.2	48.2	88.5
20	20.3	66.4	133.6	40.3	86.4	153.6
35 (RS-a03 <sup>#</sup> )	26.6	79.5	169.5	61.6	114.5	204.5
35 (RS-a07 <sup>#</sup> )	24.5	89.5	174.4	59.5	124.5	209.4
50	34.0	108.4	202.8	84.0	158.4	252.8
65	36.6	138.7	242.2	101.6	203.7	307.2
65 (RS-a10 <sup>#</sup> )	37.3	147.5	246.5	102.3	212.5	311.5
50 (RS-a08 <sup>#</sup> )	29.9	125.8	222.0	79.9	175.8	272.0
50 (RS-a09 <sup>#</sup> )	31.6	114.5	182.1	81.6	164.5	232.1
35 (RS-a15 <sup>#</sup> )	25.3	102.9	159.2	60.3	137.9	194.2

$$\sigma_{s0} = \sigma_{v0} + \sigma_3;$$

$$\sigma_{si} = \sigma_c' + \sigma_3; \sigma_{sd} = \sigma_d' + \sigma_3$$



43.2 to 147.5 MPa and  $\sigma_{v0}$  from 83.5 to 246.5 MPa. Figure 14 presents the influence of  $\sigma_3$  on  $C'$ ,  $D'$  and the stress at zero volumetric strain, together with the relationship between  $\sigma_s$  and  $\sigma_3$ . It can be seen that  $\sigma_{si}$ ,  $\sigma_{sd}$  and  $\sigma_{s0}$  all increased linearly (with good linear regression coefficients of  $R = 0.995$ – $0.998$ ) with the confining pressure. Notably, however, the  $\sigma_{s0}$  of two specimens (i.e., RS-a09<sup>#</sup> and RS-a15<sup>#</sup>) were both lower than other specimens at the same confining pressure. This is a result of reducing the confining pressure before the point of zero volumetric strain.

The sensitivity of the stress at zero volumetric strain on  $\sigma_3$  was clearly higher than that for  $D'$ , while the sensitivity of  $D'$  on  $\sigma_3$  was clearly higher than that for  $C'$ . Table 11 lists the strength parameters of red sandstone obtained using the stress at zero volumetric strain and  $D'$  and the linear Mohr-Coulomb criterion. The  $\sigma_0$  had values of 77.22 and 30.74 MPa, and  $q$  was 3.64 and 2.70 for the regression analysis using the stress at zero volumetric strain and  $D'$ , respectively. Using Eqs. 2 and 3, the values of  $c$  and  $\phi$  were calculated using the regression analysis for the stress at zero volumetric strain to be 20.24 MPa and  $34.7^\circ$ , respectively. These values were higher than the values of  $c$  and  $\phi$  (9.35 MPa and  $27.4^\circ$ ) calculated using the regression analysis for  $D'$ .

Figure 15 shows the relationship between the peak strength and  $C'$ ,  $D'$  and the stress at zero volumetric strain (from the conventional triaxial compression tests). From Fig. 15, it can be seen that with the increase of peak strength,  $C'$ ,  $D'$  and the stress at zero volumetric strain for red sandstone all increased nonlinearly. A logarithmic equation is proposed to describe the nonlinear relationship between the peak strength and the stress at zero volumetric strain,  $C'$  and  $D'$  (all of which have good nonlinear regression coefficients). By using Fig. 15, we can approximately predict the position of  $C'$ ,  $D'$  and the stress at zero volumetric strain using the peak strength of rock, even without measuring the circumferential strain curve.

#### 4.3 Failure Behavior Under Conventional Triaxial Compression and Reducing Confining Pressure

Figures 16, 17, 18, 19 and 20 show the failure modes of red sandstone specimens from our conventional triaxial compression experiments. The confining pressure had exerted a significant influence on the failure mode.

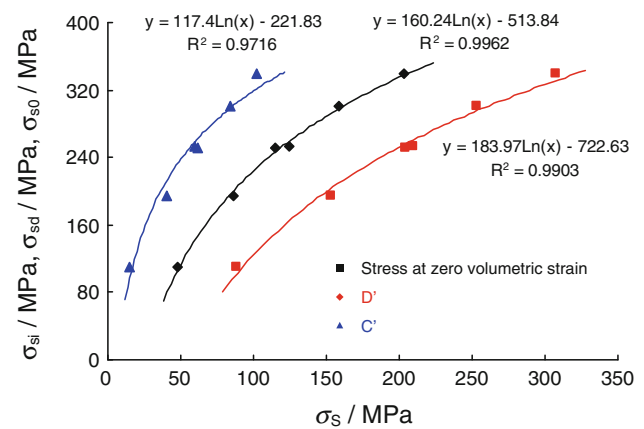


**Fig. 15** Relation between the peak strength and  $C'$ ,  $D'$  and the stress at zero volumetric strain for the conventional triaxial compression tests. The symbols represent the experimental results

At confining pressures between 5 and 20 MPa, our sandstone specimens all demonstrated a mixed tension and shear fracture mode of failure (Figs. 16, 17). Axial and lateral tensile cracks were observed at  $\sigma_3 = 5$  and 20 MPa (Figs. 16, 17). Furthermore, the widths of the tensile cracks in specimen at  $\sigma_3 = 5$  MPa were bigger than those at  $\sigma_3 = 20$  MPa. Our post-mortem specimens also indicated that it was easier for tension failure to occur at lower confining pressures. In Fig. 16, frictional sliding was also observed along the direction of the shear fracture plane. The angle of the shear fracture plane at  $\sigma_3 = 5$  MPa was approximately  $74^\circ$ , higher than for  $\sigma_3 = 20$  MPa (approximately  $68^\circ$ ).

At an intermediate confining pressure of 35 MPa, red sandstone specimens failed by the typical shear failure mode with a single fracture surface. The fracture surface was found to be very smooth and flat, which is the result of frictional sliding of the macroscopic fracture surfaces along the direction of the shear fracture plane (Fig. 18). The angle of the shear fracture plane at  $\sigma_3 = 35$  MPa was approximately  $62^\circ$ , approximately equal to that predicted using the linear Mohr-Coulomb criterion [i.e.,  $63^\circ$  ( $45^\circ + \phi/2$ )].

However, at higher confining pressures of 50 and 65 MPa, the failure modes of red sandstone were different. At  $\sigma_3 = 50$  MPa, the sandstone exhibited a shear failure mode, with several closed shear bands (Fig. 19) and a shear fracture angle of approximately  $57^\circ$ . The shear frictional

**Table 11** Strength parameters of red sandstone obtained using  $C'$ ,  $D'$  and the stress at zero volumetric strain by the linear Mohr-Coulomb criterion

Different regression analysis	$\sigma_0$ /MPa	$q$	$c$ /MPa	$\phi/^\circ$	$R$
Using the stress at zero volumetric strain	77.22	3.64	20.24	34.7	0.995
Using $D'$	30.74	2.70	9.35	27.4	0.995
Using $C'$	10.15	1.43	4.24	10.2	0.998

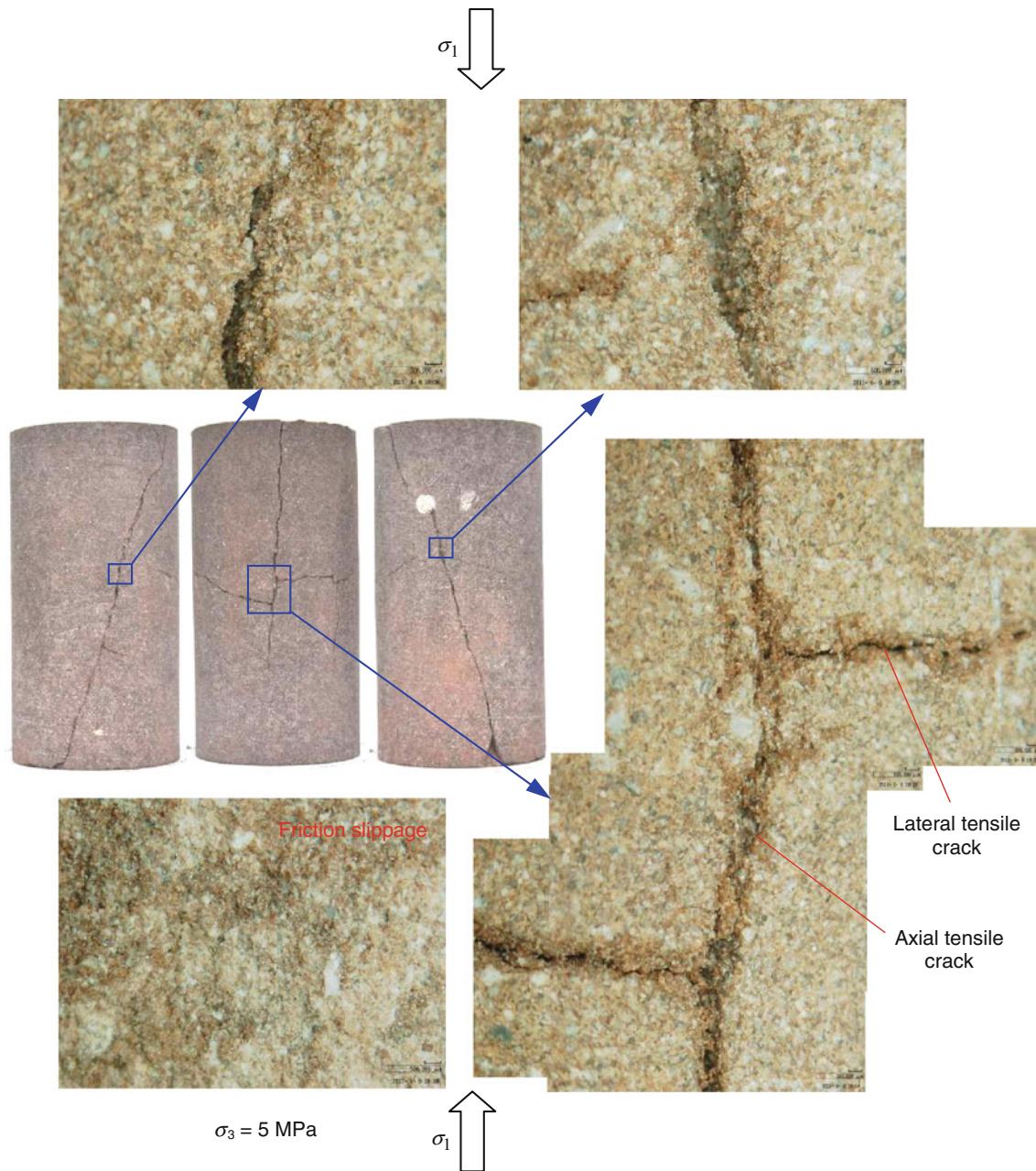


**Fig. 16** Mixed tension and shear fracture mode of red sandstone from a conventional triaxial compression experiment at a confining pressure of 5 MPa

sliding was distinct, and the direction of sliding was along the shear fracture plane. At  $\sigma_3 = 65$  MPa, the sandstone exhibited a shear failure mode with double slippage planes (Fig. 20), and the angle of the shear fracture plane was approximately  $55^\circ$ . It should be noted that the shear fracture surfaces under higher confining pressures of 50 and 65 MPa were not as smooth as for  $\sigma_3 = 35$  MPa. A closed shear band and an open shear fracture were both observed for  $\sigma_3 = 65$  MPa. A considerable amount of fault gouge, a

result of the frictional sliding along the shear fracture planes, was also observed (the direction of frictional sliding was also along the shear fracture plane). The angle of the shear fracture plane at  $\sigma_3 = 50$  and 65 MPa was lower than  $63^\circ$  (i.e.,  $45^\circ + \phi/2$ ), as predicted using the linear Mohr-Coulomb criterion.

For our “reducing confining pressure” experiments, the failure mode of red sandstone (Fig. 21) was significantly different from that obtained in our conventional triaxial



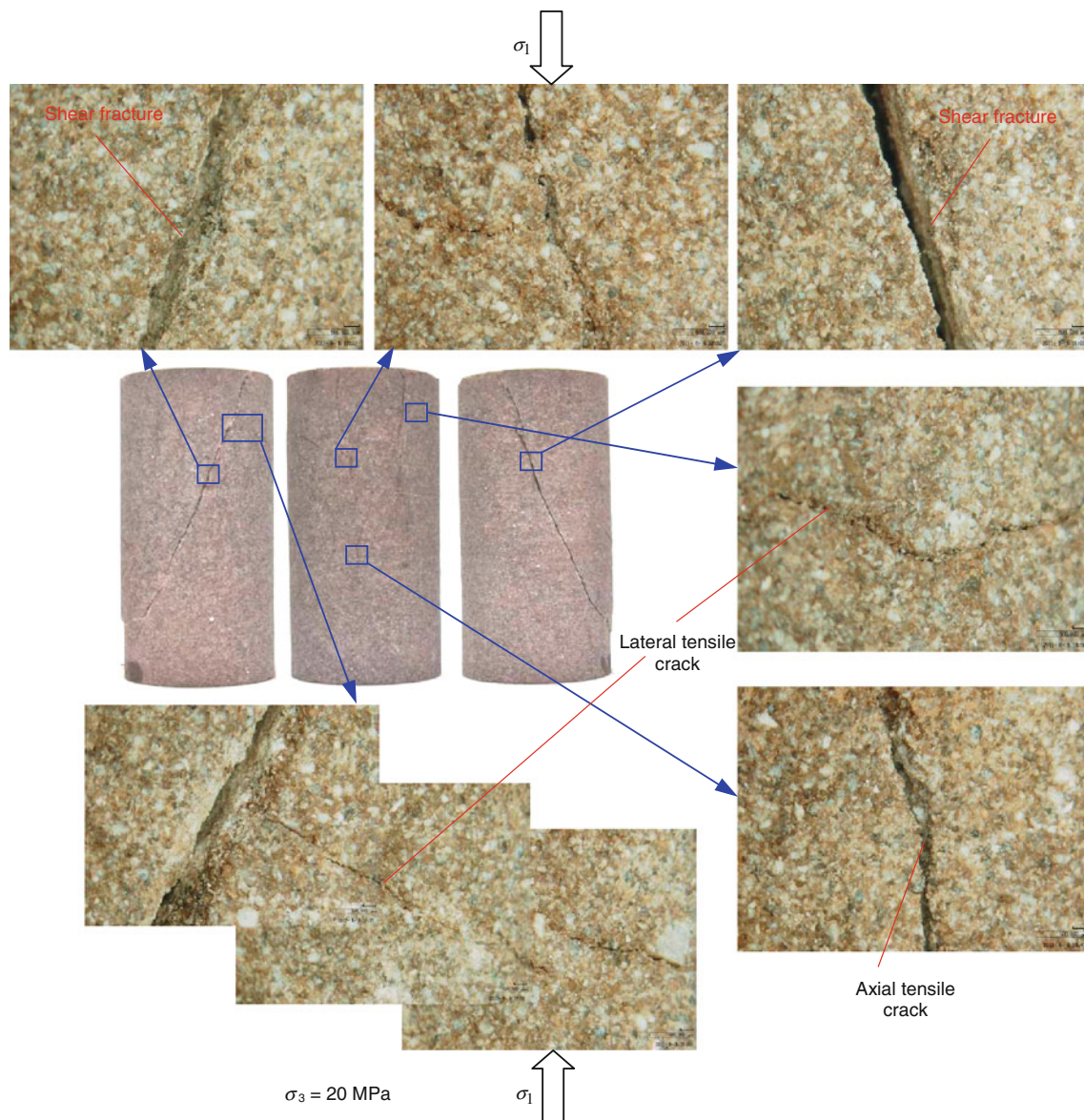


**Fig. 17** Mixed tension and shear fracture mode of red sandstone from a conventional triaxial compression experiment at a confining pressure of 20 MPa

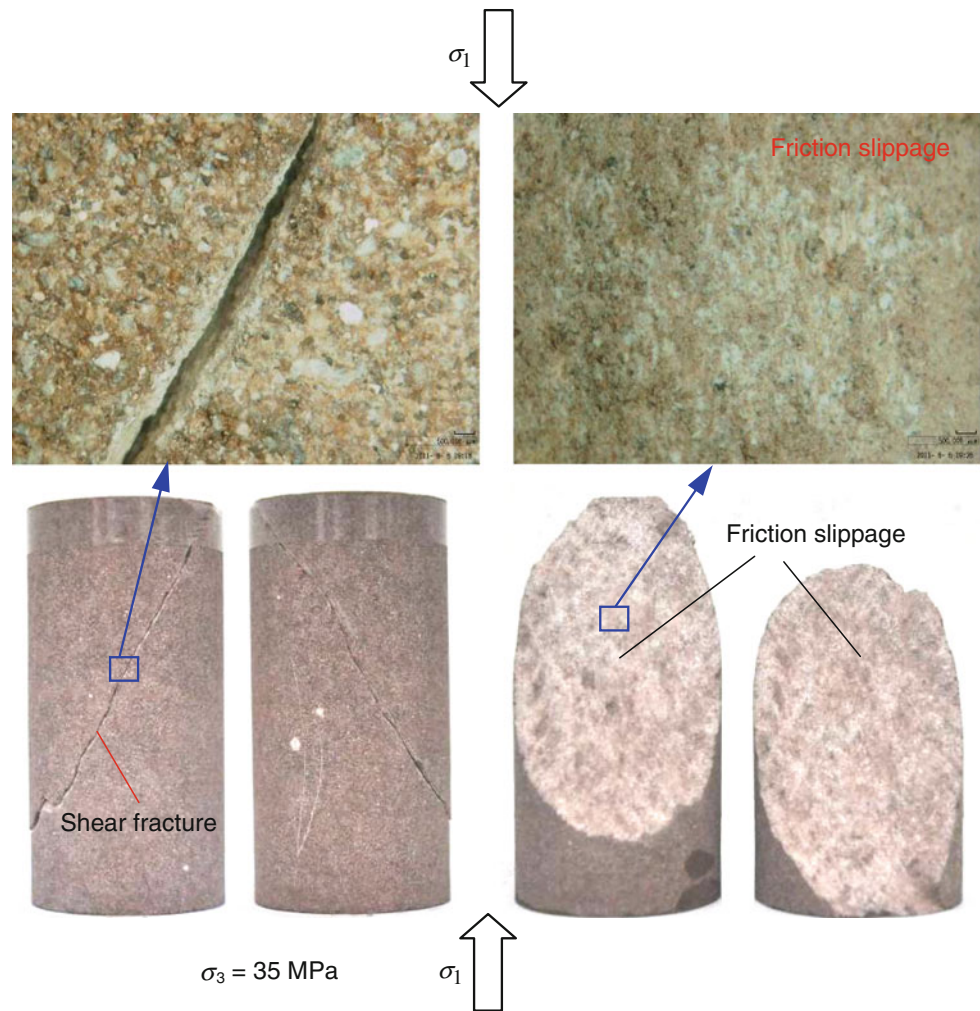
compression experiments; it was much more complex. Further, the width of the fracture surfaces appeared to be greatly increased.

At  $\sigma_{3i} = 65$  MPa and  $\sigma_{3f} = 48.7$  MPa, the sandstone exhibited a shear fracture failure mode with local tensile cracks. The angle of the shear fracture plane was approximately  $57^\circ$ . At  $\sigma_{3i} = 50$  MPa and  $\sigma_{3f} = 36.8$  MPa, a more complicated failure mode was observed (Fig. 21b). The main failure mode of specimen RS-a08<sup>#</sup> was by a shear fracture (e.g., 1–3 on Fig. 21b). Shear fracture plane 1 was the reverse of shear fracture plane 2, while shear fracture plane 2 was linked with shear fracture plane 3.

Furthermore, in specimen RS-a08<sup>#</sup>, some axial and lateral tensile cracks were also observed, perhaps due to decreasing the confinement on the specimen.

We also saw a complicated failure mode at  $\sigma_{3i} = 50$  MPa and  $\sigma_{3f} = 24.5$  MPa (Fig. 21c). From Fig. 21c, the main failure mode of specimen RS-a09<sup>#</sup> was also by means of a shear fracture. Shear fracture plane 1 was the reverse of shear fracture plane 3, while shear fracture plane 2 was linked with shear fracture plane 1. Tensile cracks were again observed (see a and b in Fig. 22). The initial confining pressure of two specimens, RS-a08<sup>#</sup> and RS-a09<sup>#</sup>, was the same, but the final confining pressure upon failure for specimen RS-a09<sup>#</sup> was

**Fig. 18** Single shear fracture mode of red sandstone from a conventional triaxial compression experiment at a confining pressure of 35 MPa



lower. Therefore, in specimen RS-a09<sup>#</sup>, more small tensile cracks were required to initiate the process of final failure.

At  $\sigma_{3i} = 35$  MPa and  $\sigma_{3f} = 17$  MPa, the sandstone primarily took on a shear failure mode with a single shear fracture plane. However, at the point of localization, there were some axial and lateral tensile cracks (see C and D in Fig. 22). Again, these are likely to be the result of the specimen failing by reducing the confining pressure; they were not observed in the specimens from the conventional triaxial compression experiments.

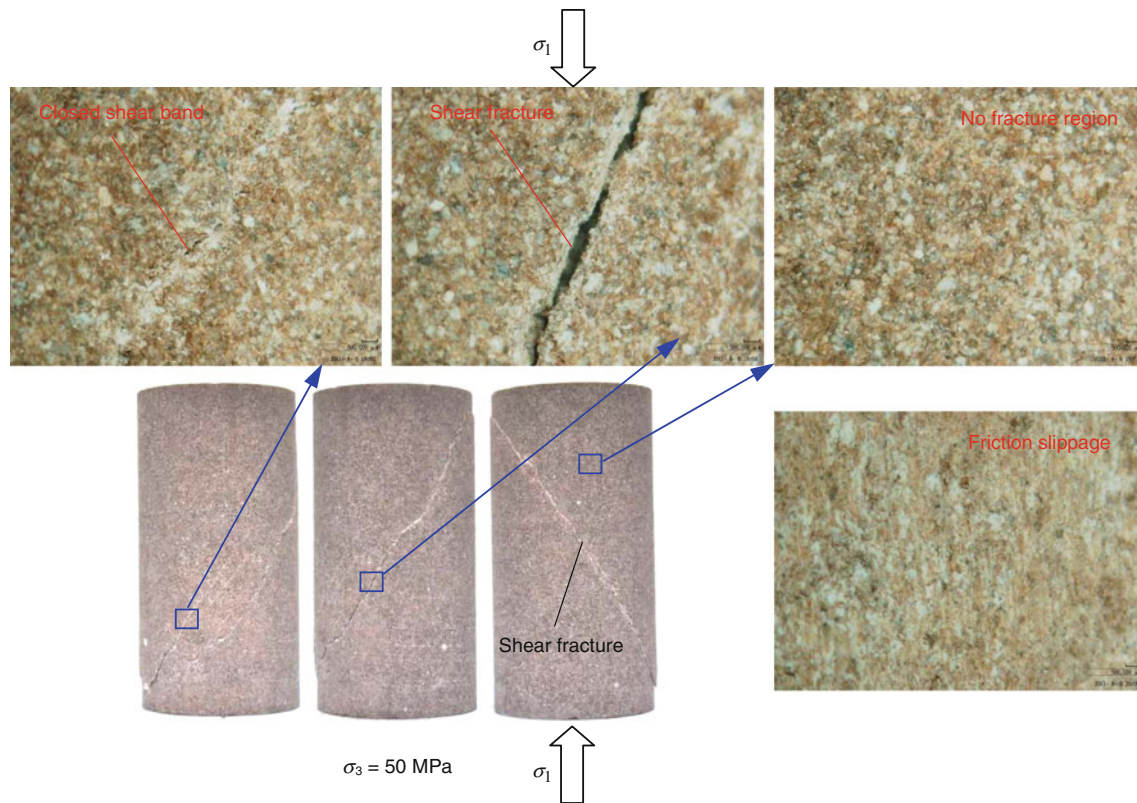
## 5 Spatial AE Locations Behavior

Figure 23 shows the relationship between axial deviatoric stress, AE counts and the strain of red sandstone at a confining pressure of 35 MPa. Figure 24 shows the spatial AE locations behavior for the same experiment;

the letters shown in Fig. 24 correspond to the time slices of Fig. 23.

Using Figs. 23 and 24, we can analyze the coalescence process of internal cracks in red sandstone during triaxial compression. When the axial deviatoric stress was loaded to points a and b, the AE counts in the specimen were very rare, and they resulted from small micro-failure occurrences during elastic deformation. With increasing circumferential deformation, the axial deviatoric stress-strain curve began to depart from the domain of elastic deformation. When the axial deviatoric stress reached point c ( $\sigma_1 - \sigma_3 = 189.4$  MPa = 87.6% $\sigma_p$ ,  $\varepsilon_1 = 4.41 \times 10^{-3}$ ), the AE counts in the specimen reached 80, which meant that the specimen contained a small amount of internal damage. When the specimen was loaded to point d ( $\sigma_1 - \sigma_3 = 208.2$  MPa = 96.3% $\sigma_p$ ,  $\varepsilon_1 = 5.21 \times 10^{-3}$ ), the AE counts within the specimen reached 149, indicating that more microcracking took place within the specimen. Before point d, the AE counts were located in the top and





**Fig. 19** Shear fracture mode with local slippage lines of red sandstone from a conventional triaxial compression experiment at a confining pressure of 35 MPa

bottom regions of the specimen, and there were almost no AE counts in the central region of the specimen.

When the axial deviatoric stress was loaded to point e ( $\sigma_1 - \sigma_3 = 214.7 \text{ MPa} = 99.4\% \sigma_p$ ,  $\varepsilon_1 = 5.75 \times 10^{-3}$ ), the AE counts reached 207 in the specimen. There were also some AE counts in the central region of the specimen. Once the specimen had reached point f ( $\sigma_1 - \sigma_3 = 216.1 \text{ MPa} = 100\% \sigma_p$ ,  $\varepsilon_1 = 6.10 \times 10^{-3}$ ), the AE counts in the specimen totaled 267. The AE counts were now accumulating throughout the entire specimen. However, the specimen was still macroscopically coherent, even though it had some internal damage failure. After the peak strength, from point f to j, the axial deviatoric stress on the specimen slowly dropped from 216.1 to 207.9 MPa as the circumferential strain increased from  $6.22 \times 10^{-3}$  to  $10.27 \times 10^{-3}$  (Fig. 23), but the axial strain of the specimen only increased to  $7.17 \times 10^{-3}$  from  $6.10 \times 10^{-3}$ . During the reduction of axial deviatoric stress from point f to j, even though it involved a small stress drop, the circumferential deformation of the specimen was increasing faster than the axial deformation (indicating that there was a large amount of dilatancy). The AE counts increased to 926 at point j, and more AE events were observed throughout the specimen (Fig. 24j).

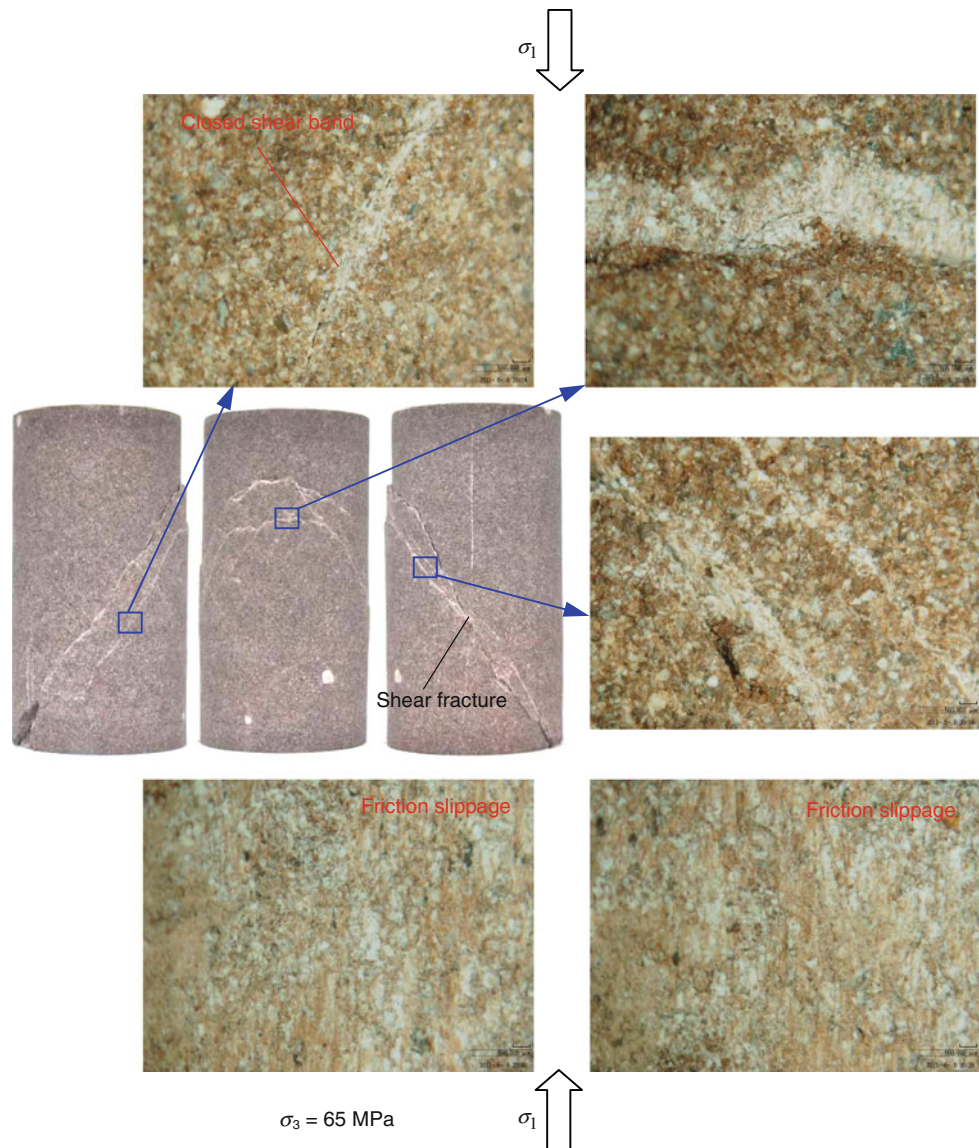
Between point j and point k, the axial deviatoric stress significantly decreased from 207.9 to 196.4 MPa, and the axial strain slightly increased from  $7.17 \times 10^{-3}$  to  $7.39 \times 10^{-3}$ . However, the accumulated AE counts in the specimen increased rapidly to 1,883. At this moment, the specimen experienced a serious damage failure. The axial stress dropped rapidly to 140.2 from 196.4 MPa upon reaching point l, and the AE counts increased to 3,056. The main failure mode with the single shear fracture plane could be seen from the elliptical region in Fig. 24l. The axial deviatoric stress was then loaded to point m ( $\sigma_1 - \sigma_3 = 113.2 \text{ MPa}$ ,  $\varepsilon_1 = 11.15 \times 10^{-3}$ ), and the specimen was located at the stage of residual strength. At this time, the AE counts from the specimen reached 3,843, and the macroscopic shear fracture plane was initiated, which could be observed from Fig. 24m. The failure mode of the specimen formed by AE location analysis showed good agreement with the experimental failure mode.

## 6 Conclusions

We have presented an experimental investigation of the strength, deformation behavior, failure characteristics and



**Fig. 20** Shear fracture mode with double slippage planes of red sandstone from a conventional triaxial compression experiment at a confining pressure of 65 MPa



spatial AE locations of red sandstone under triaxial compression. In our study, we used the circumferential displacement as the controlling feedback signal (as opposed to the more usual axial displacement feedback) to obtain better triaxial compression experimental results for red sandstone. Based on our data, the following conclusions can be drawn.

1. Our results show that the post-peak axial deformation of red sandstone was changed as the confining pressure was increased from 5 to 65 MPa. Young's modulus increased nonlinearly with confining pressure, but Poisson's ratio remained unchanged. In the range of tested  $\sigma_3$  (from 5 to 65 MPa), Poisson's ratio ranged from 0.28 to 0.37, and the average Poisson's ratio was approximately 0.33.
2. According to the observed compactive and dilatancy behavior, the influence of the confining pressure on the corresponding deformation parameters of red sandstone can be discussed further. The peak axial strain increased linearly with the confining pressure, but the peak circumferential strain only showed a modest increase. However, during our "reducing confining pressure" experiments, the peak strain showed no clear linear relation, especially for the peak circumferential strain. In addition, the peak strain during our "reducing confining pressure" experiments was higher than that for our conventional triaxial compression experiments for the same confining pressure. The axial and circumferential strain at  $C'$ ,  $D'$  and the stress at zero volumetric strain all increased nonlinearly with the

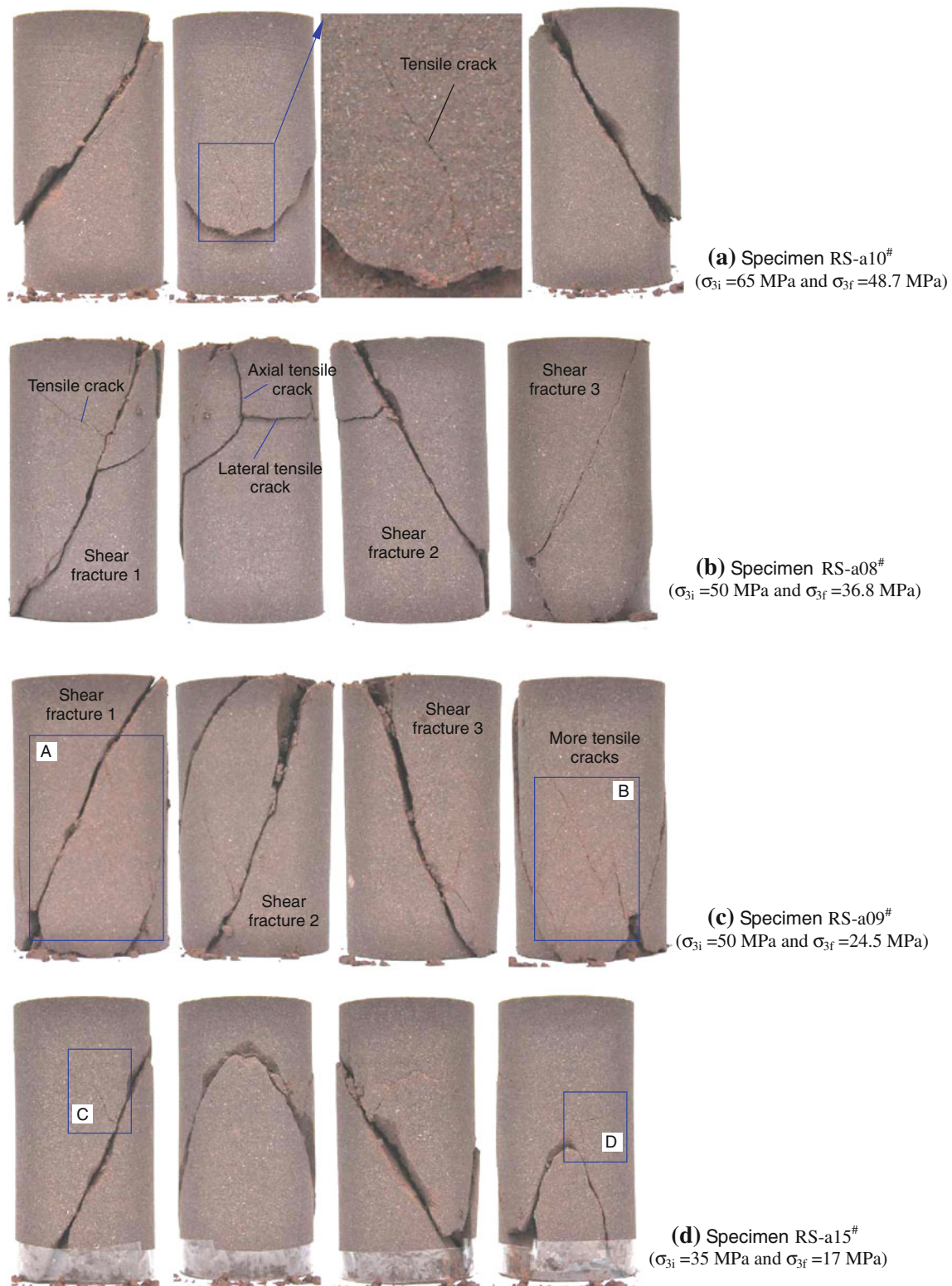


**Fig. 21** Failure mode of red sandstone deformed in “reducing confining pressure” experiments with different initial conditions

confining pressure. However, the  $\varepsilon_{3c'}$ ,  $\varepsilon_{3d'}$  and  $\varepsilon_{3v0}$  increased linearly with increasing  $\varepsilon_{1c'}$ ,  $\varepsilon_{1d'}$  and  $\varepsilon_{1v0}$ , respectively.

3. The strength and failure behavior of red sandstone under triaxial compression can also be analyzed. The nonlinear Hoek-Brown criterion better reflected the

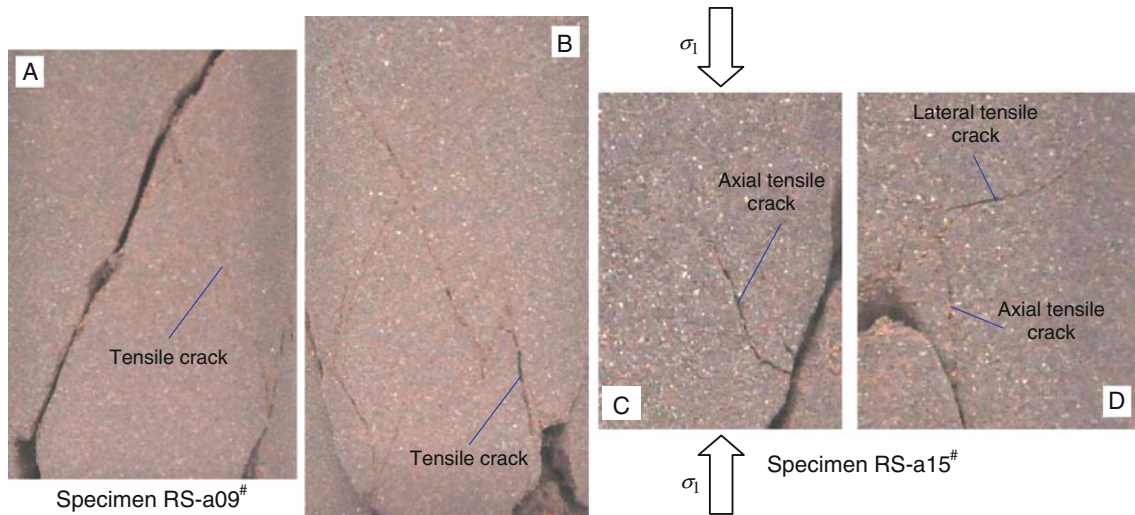
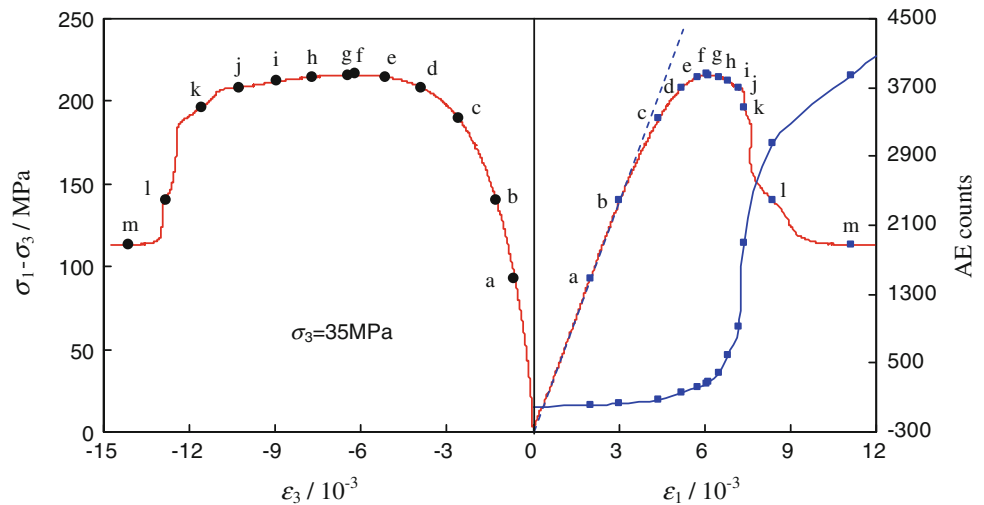


**Fig. 22** Local magnification of tensile cracks in red sandstone from “reducing confining pressure” experiments. The denoted letters a–d correspond to those in Fig. 21

**Fig. 23** Relationship between axial differential stress, AE counts and strain for red sandstone at a confining pressure of 35 MPa



peak strength properties than the linear Mohr-Coulomb criterion. However, even though there was an obvious non-linear relationship between the peak strength and the confining pressure, the residual strength of red sandstone exhibited a clear linear relationship with the confining pressure (best described using the linear Mohr-Coulomb criterion). The peak and residual strengths were not directly related to two different loading paths.  $C'$ ,  $D'$  and the stress at zero volumetric strain all increased linearly with confining pressure. The strength parameters obtained using  $C'$  and  $D'$  were obviously lower than those obtained by the peak strength.

4. In our conventional triaxial compression experiments, with increasing confining pressure, the failure mode of red sandstone changed from mixed tension and shear fracture (single shear fracture) to shear fracture with double slippage planes. However, the failure mode in our “reducing confining pressure” experiments was found to be more complicated, which results mainly from the unstable failure characteristics of the rock during the reduction in confining pressure.
5. Finally, based on the obtained spatial AE locations at a confining pressure of 35 MPa, a detailed analysis of the evolutionary process of internal cracks in red



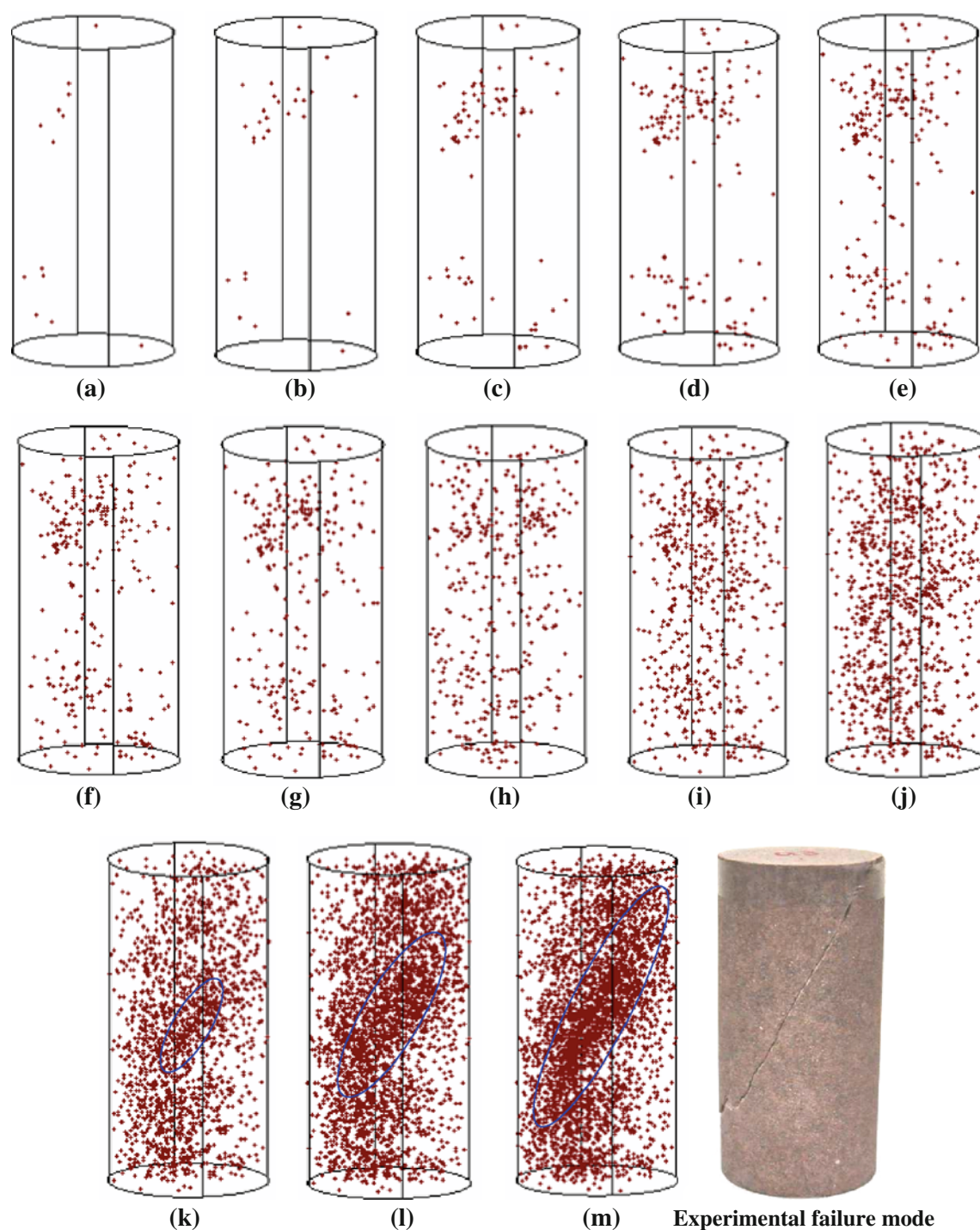


**Fig. 24** Spatial AE locations behavior for red sandstone at a confining pressure of 35 MPa. The denoted *letters* shown in the figure correspond to those on the stress-strain curve in Fig. 23

sandstone was established for the entire loading process. These results may be significant for predicting and forecasting failure processes in the field of deep underground rock mass engineering.

**Acknowledgments** This research was supported by the National Natural Science Foundation of China (grant no. 51179189, 51074162), a China Postdoctoral Science Foundation specially funded project (grant no. 201104585) and a Qing Lan Project of Jiangsu Province (2010). We also would like to express our sincere gratitude

to the editor, two anonymous reviewers and Mike Heap for their valuable comments, which have greatly improved this paper.

## References

- Al-Harthi AA (1998) Effect of planar structures on the anisotropy of Ranyah sandstone Saudi Arabia. *Eng Geol* 50(1/2):49–57
- Alkan H, Cinar Y, Pusch G (2007) Rock salt dilatancy boundary from combined acoustic emission and triaxial compression tests. *Int J Rock Mech Min Sci* 44(1):108–119
- Amann F, Button EA, Evans KF, Gischig VS, Blumel M (2011) Experimental study of the brittle behavior of clay shale in rapid unconfined compression. *Rock Mech Rock Eng* 44(4):415–430
- Bagde MN, Petroš V (2005) Fatigue properties of intact sandstone specimens subjected to dynamic uniaxial cyclical loading. *Int J Rock Mech Min Sci* 42(2):237–250
- Bell AF, Greenough J, Heap MJ, Main IG (2011a) Challenges for forecasting based on accelerating rates of earthquakes at volcanoes and laboratory analogues. *Geophys J Int* 185(2):718–723
- Bell AF, Naylor M, Heap MJ, Main IG (2011b) Forecasting volcanic eruptions and other material failure phenomena: an evaluation of the failure forecast method. *Geophys Res Lett.* doi:[10.1029/2011GL048155](https://doi.org/10.1029/2011GL048155)
- Bésuelle P, Desrues J, Raynaud S (2000) Experimental characterization of the localisation phenomenon inside a Vosges sandstone in a triaxial cell. *Int J Rock Mech Min Sci* 37(8):1223–1237
- Bésuelle P, Baud P, Wong TF (2003) Failure mode and spatial distribution of damage in Rothbach sandstone in the brittle–ductile transition. *Pure Appl Geophys* 160(5/6):851–868
- Baud P, Zhu W, Wong TF (2000) Failure mode and weakening effect of water on sandstone. *J Geophys Res* 105((B7)):16371–16389
- Baud P, Klein E, Wong TF (2004) Compaction localization in porous sandstones: spatial evolution of damage and acoustic emission activity. *J Struct Geol* 26(4):603–624
- Benson PM, Meredith PG, Platzman ES, White RE (2005) Pore fabric shape anisotropy in porous sandstones and its relation to elastic wave velocity and permeability anisotropy under hydrostatic pressure. *Int J Rock Mech Min Sci* 42(7/8):890–899
- Benson PM, Thompson AB, Meredith PG, Vinciguerra S, Young RP (2007) Imaging slow failure in triaxially deformed Etna basalt using 3D acoustic-emission location and X-ray computed tomography. *Geophys Res Lett.* doi:[10.1029/2006GL028721](https://doi.org/10.1029/2006GL028721)
- Brantut N, Schubnel A, Guéguen Y (2011) Damage and rupture dynamics at the brittle-ductile transition: the case of gypsum. *J Geophys Res* 116:B01404. doi:[10.1029/2010JB007675](https://doi.org/10.1029/2010JB007675)
- Chang SH, Cl Lee (2004) Estimation of cracking and damage mechanisms in rock under triaxial compression by moment tensor analysis of acoustic emission. *Int J Rock Mech Min Sci* 41(7):1069–1086
- Fairhurst CE, Hudson JA (1999) Draft ISRM suggested method for the complete stress–strain curve for the intact rock in uniaxial compression. *Int J Rock Mech Min Sci* 36(3):279–289
- Feng XT, Chen SL, Zhou H (2004) Real-time computerized tomography (CT) experiments on sandstone damage evolution during triaxial compression with chemical corrosion. *Int J Rock Mech Min Sci* 41(2):181–192
- Fortin J, Stanchits S, Dresen G, Gueguen Y (2006) Acoustic emission and velocities associated with the formation of compaction bands in sandstone. *J Geophys Res.* doi:[10.1029/2005JB003854](https://doi.org/10.1029/2005JB003854)
- Fortin J, Stanchits S, Dresen G, Gueguen Y (2009) Acoustic emissions monitoring during inelastic deformation of porous sandstone: comparison of three modes of deformation. *Pure Appl Geophys* 166(5–7):823–841
- Hawkes I, Mellor M (1970) Uniaxial testing in rock mechanics laboratories. *Eng Geol* 4:177–285
- Heap MJ, Baud P, Meredith PG, Bell AF, Main IG (2009a). Time-dependent brittle creep in Darley Dale sandstone. *J Geophys Res.* doi:[10.1029/2008JB006212](https://doi.org/10.1029/2008JB006212)
- Heap MJ, Baud P, Meredith PG (2009b) The influence of temperature on brittle creep in sandstones. *Geophys Res Lett.* doi:[10.1029/2009GL039373](https://doi.org/10.1029/2009GL039373)
- Heap MJ, Faulkner DR, Meredith PG, Vinciguerra S (2010) Elastic moduli evolution and accompanying stress changes with increasing crack damage: implications for stress changes around fault zones and volcanoes during deformation. *Geophys J Int* 183:225–236
- Hoek E, Brown ET (1980) Underground excavation in rock. Institution of Mining and Metallurgy, London
- Hoek E, Brown ET (1997) Practical estimates of rock mass strength. *Int J Rock Mech Min Sci* 34(8):1165–1186
- Huang S, Xia KW, Yang F, Feng XT (2010) An experimental study of the rate dependence of tensile strength softening of Longyou sandstone. *Rock Mech Rock Eng* 43(6):677–683
- Jeng FS, Weng MC, Huang TH, Lin ML (2002) Deformational characteristics of weak sandstone and impact to tunnel deformation. *Tunnel Undergr Space Technol* 17(3):263–274
- Klein E, Baud P, Reuschle T, Wong TF (2001) Mechanical behaviour and failure mode of Bentheim sandstone under triaxial compression. *Phys Chem Earth (A)* 26:21–25
- Lin Q, Fakhimi A, Haggerty M, Labuz JF (2009) Initiation of tensile and mixed-mode fracture in sandstone. *Int J Rock Mech Min Sci* 46(3):489–497
- Lockner D, Byerlee J, Kuksenko V, Ponomarev A, Sidorin A (1991) Quasi-static fault growth and shear fracture energy in granite. *Nature* 350:39–42
- Mogi K (1966) Some precise measurements of fracture strength of rocks under uniform compressive stress. *Rock Mech Eng Geol* 4:41–55
- Mohr O (1914) *Abhandlungen aus dem Gebiete der Technischen Mechanik*, second edn. Ernst, Berlin
- Nespereira J, Blanco JA, Yenes M, Pereira D (2010) Irregular silica cementation in sandstones and its implication on the usability as building stone. *Eng Geol* 115(3/4):167–174
- Paterson MS, Wong TF (2005) *Experimental rock deformation—the brittle field*. Springer, New York
- Pestman BJ, Van Munster JG (1996) An acoustic emission study of damage development and stress-memory effects in sandstone. *Int J Rock Mech Min Sci Geomech Abstr* 33(6):585–593
- Rutter E (1986) On the nomenclature of mode of failure transitions in rocks. *Tectonophysics* 122:381–387
- Tembe S, Baud P, Wong TF (2008) Stress conditions for the propagation of discrete compaction bands in porous sandstone. *J Geophys Res.* doi:[10.1029/2007JB005439](https://doi.org/10.1029/2007JB005439)
- Townend E, Thompson BD, Benson PM, Meredith PG, Baud P, Young RP (2008) Imaging compaction band propagation in Diemelstadt sandstone using acoustic emission locations. *Geophys Res Lett.* doi:[10.1029/2008GL034723](https://doi.org/10.1029/2008GL034723)
- Tsai LS, Hsieh YM, Weng MC, Huang TH, Jeng FS (2008) Time-dependent deformation behaviors of weak sandstones. *Int J Rock Mech Min Sci* 45(2):144–154
- Tavallali A, Vervoort A (2010) Effect of layer orientation on the failure of layered sandstone under Brazilian test conditions. *Int J Rock Mech Min Sci* 47(2):313–322
- Wawersik WR, Fairhurst C (1970) A study of brittle rock fracture in laboratory compression experiments. *Int J Rock Mech Min Sci* 7:561–575
- Wong TF, David C, Zhu W (1997) The transition from brittle faulting to cataclastic flow in porous sandstones: Mechanical deformation. *J Geophys Res* 102((B2)):3009–3025



- Wu XY, Baud P, Wong TF (2000) Micromechanics of compressive failure and spatial evolution of anisotropic damage in Darley Dale sandstone. *Int J Rock Mech Min Sci* 37(1/2):143–160
- Yang SQ, Jiang YZ (2010) Triaxial mechanical creep behavior of sandstone. *Min Sci Technol* 20(3):339–349
- Yang SQ, Jing HW (2011) Strength failure and crack coalescence behavior of brittle sandstone samples containing a single fissure under uniaxial compression. *Int J Fract* 168(2):227–250
- Yang SQ, Jing HW, Li YS, Han LJ (2011) Experimental investigation on mechanical behavior of coarse marble under six different loading paths. *Exp Mech* 51(3):315–334
- Youn H, Tonon F (2010) Multi-stage triaxial test on brittle rock. *Int J Rock Mech Min Sci* 47(4):678–684
- Zorlu K, Gokceoglu C, Ocakoglu F, Nefelioglu HA, Acikalin S (2008) Prediction of uniaxial compression strength of sandstones using petrography-based models. *Eng Geol* 96(3/4):141–158